Acta Neuropathologica (2019) 138:103–121
https://doi.org/10.1007/s00401-019-01989-y

ORIGINAL PAPER

ALS/FTD mutant CHCHD10 mice reveal a tissue-specific toxic gain-of-function and mitochondrial stress response

Corey J. Anderson[1] · Kirsten Bredvik[1] · Suzanne R. Burstein[1] · Crystal Davis[2] · Samantha M. Meadows[1,3] · Jalia Dash[1] · Laure Case[2] · Teresa A. Milner[1,4] · Hibiki Kawamata[1] · Aamir Zuberi[2] · Alessandra Piersigilli[5] · Cathleen Lutz[2] · Giovanni Manfredi[1]

Received: 14 December 2018 / Revised: 25 February 2019 / Accepted: 8 March 2019 / Published online: 14 March 2019
© Springer-Verlag GmbH Germany, part of Springer Nature 2019

Abstract

Mutations in coiled-coil-helix–coiled-coil-helix domain containing 10 (CHCHD10), a mitochondrial protein of unknown function, cause a disease spectrum with clinical features of motor neuron disease, dementia, myopathy and cardiomyopathy. To investigate the pathogenic mechanisms of CHCHD10, we generated mutant knock-in mice harboring the mouse-equivalent of a disease-associated human S59L mutation, S55L in the endogenous mouse gene. CHCHD10^{S55L} mice develop progressive motor deficits, myopathy, cardiomyopathy and accelerated mortality. Critically, CHCHD10 accumulates in aggregates with its paralog CHCHD2 specifically in affected tissues of CHCHD10^{S55L} mice, leading to aberrant organelle morphology and function. Aggregates induce a potent mitochondrial integrated stress response (mtISR) through mTORC1 activation, with elevation of stress-induced transcription factors, secretion of myokines, upregulated serine and one-carbon metabolism, and downregulation of respiratory chain enzymes. Conversely, CHCHD10 ablation does not induce disease pathology or activate the mtISR, indicating that CHCHD10^{S55L}-dependent disease pathology is not caused by loss-of-function. Overall, CHCHD10^{S55L} mice recapitulate crucial aspects of human disease and reveal a novel toxic gain-of-function mechanism through maladaptive mtISR and metabolic dysregulation.

Keywords CHCHD10 · CHCHD2 · Knock-in mice · ALS · FTD · Mitochondrial myopathy · Neurodegeneration · Protein aggregation · Mitochondrial integrated stress response

Introduction

Mitochondria are essential organelles that mediate vital cellular processes including energy metabolism, calcium handling, and cell death programs. Mitochondrial function is particularly important in energy-demanding tissues, such as the nervous system, heart, and muscle. Genetic mutations affecting mitochondria cause a multitude of inherited metabolic diseases in humans. However, while mitochondrial dysfunction has been often described in chronic neurodegenerative disorders, including Alzheimer's and Parkinson's disease (PD) and amyotrophic lateral sclerosis (ALS), the primary causes of this dysfunction are largely unknown and sometimes controversial [17]. Mitochondria are often considered targets rather than triggers of neurodegeneration. However, a new twist in the mitochondrial origin of neurodegeneration saga has come from the recent discovery of mutations in the coiled-coil-helix–coiled-coil-helix domain containing 10 (*CHCHD10*) gene, causing ALS, frontotemporal dementia (FTD), PD, Charcot–Marie–Tooth

Electronic supplementary material The online version of this article (https://doi.org/10.1007/s00401-019-01989-y) contains supplementary material, which is available to authorized users.

✉ Giovanni Manfredi
gim2004@med.cornell.edu

1 Feil Family Brain and Mind Research Institute, Weill Cornell Medicine, 407 East 61st Street, New York, NY 10065, USA

2 The Rare and Orphan Disease Center, JAX Center for Precision Genetics, 600 Main Street, Bar Harbor, ME 04609, USA

3 Neuroscience Graduate Program, Weill Cornell Graduate School of Medical Sciences, 1300 York Ave, New York, NY 10065, USA

4 Harold and Margaret Milliken Hatch Laboratory of Neuroendocrinology, The Rockefeller University, New York, USA

5 Tri-Institutional Laboratory of Comparative Pathology, Memorial Sloan Kettering Cancer Center, Weill Cornell Medicine, and The Rockefeller University, New York, NY 10065, USA

disease, myopathy, and cardiomyopathy [1, 11, 29]. Therefore, CHCHD10 mutations cause primary mitochondrial neurodegenerative diseases, but the disease mechanisms remain largely unknown.

CHCHD10 belongs to a family of twin CX_9C proteins that are imported into the intermembrane space of mitochondria by the Mia40 disulfide relay system [5]. In mitochondria, CHCHD10 dimerizes with its paralog CHCHD2 in complexes associated with the inner mitochondrial membrane [4, 35]. The expression of CHCHD10 and CHCHD2 appears to be highly coordinated in tissues [1, 4]. CHCHD10 is strongly expressed in muscle and heart and in specific cell types of the central nervous system (CNS), including dopaminergic neurons of the midbrain and motor neurons in the spinal cord [1, 4, 15]. Although the normal roles of CHCHD10 and CHCHD2 remain unknown, both proteins have short half-lives [4, 30, 35], suggesting that they may have signaling or transport, rather than structural, functions.

In vitro studies have provided divergent conclusions about disease mechanisms in CHCHD10 mutants. Loss of function by haploinsufficiency has been proposed for some mutations [3, 13, 35], but gain-of-function mechanisms have also been suggested [21, 39]. Importantly, ablation of CHCHD10 in mice has very little effect on mitochondrial function and does not produce a disease phenotype [4], suggesting that a gain-of-function mechanism is more likely in CHCHD10 patients.

$CHCHD10^{S59L}$ was the first mutation reported in humans [1] and is the most widely studied [1, 4, 13]. To model $CHCHD10^{S59L}$ disease in vivo and study its pathogenic mechanisms, we generated a knock-in mouse harboring the murine equivalent of the human S59L mutation ($CHCHD10^{S55L}$). We find that $CHCHD10^{S55L}$ mice develop a severe neuromuscular and cardiac disease and die prematurely. Although the mutant protein is expressed in all tissues, only the affected tissues exhibit mitochondrial protein aggregates, which correlate with mitochondrial ultrastructural damage and chronic induction of the integrated mitochondrial stress response (mtISR). Conversely, CHCHD10 knockout (KO) mice containing a 1 nt insertion in exon 2 resulting in a prematurely terminated protein (C57BL/6J-$Chchd10^{em5Lutzy}$/J, Stock #028694) do not have decreased lifespan, pathological abnormalities, or induction of the mtISR. These results demonstrate for the first time in vivo that $CHCHD10^{S55L}$ causes disease through a tissue-specific toxic gain-of-function mechanism that triggers protein aggregation and maladaptive mtISR.

Materials and methods

Animal studies

All animal procedures were approved by the Weill Cornell Medicine or Jackson Laboratory Animal Care and Use Committee and were performed according to the Guidelines for the Care and Use of Laboratory Animals of the National Institutes of Health. CRISPR/Cas9 endonuclease-mediated genome editing of the *Chchd10* gene was used to introduce the S55L knock-in mutation (TCA → TTA codon change) via homologous-directed repair using a mutagenic oligonucleotide into the C57BL/6NJ inbred mouse strain (available as Stock #005304 from the Jackson Laboratory; http://www.jax.org). The sgRNA, mutagenic oligonucleotide and the *Cas9* nuclease were introduced into C57BL/6NJ-derived fertilized eggs containing well-recognized pronuclei. The sgRNA used was homologous to *Chchd10* exon 2 (exon 2 of transcript 201; exon 3 of transcript 203—Ensembl nomenclature), TAGCCGTGGGCTCAGCTGTA adjacent to a GGG PAM sequence. Targeted zygotes were transferred to pseudopregnant females. Genomic DNA from the resulting potential founder mice was amplified and sequenced using PCR primers flanking exon 2 of *Chchd10*. Sixteen founders were recovered, of which one successfully transmitted the S55L mutation to N1 progeny when backcrossed to C57BL/6NJ. This strain (Jackson Laboratory Stock #028952—C57BL/6NJ-$Chchd10^{em8Lutzy}$/J) was backcrossed once more to C57BL/6NJ before characterization.

Body weight was measured weekly starting at 125 days of age. The age of death or the age at which institutional guidelines required euthanasia was recorded for each animal and used to construct a Kaplan–Meier survival curve.

Forepaw muscle strength was measured using a digital grip-strength meter (Columbus Instruments). Animals were trained to grasp a horizontal grasping ring. During the testing phase, the average of three trials recorded at 5-min intervals was recorded per mouse.

Endurance was measured weekly as time to fatigue on a conventional treadmill running task. After two training sessions, mice were placed on a treadmill (Columbus Instruments) with a speed starting at a 10 m/min increasing incrementally by 1 m every 3 min to a maximum of 18 m/min, at a fixed incline of 5%. The treadmill was equipped with a motivational grid. The test ended when mice were unable to maintain pace despite reinforcement.

The pole task was used to assess movement deficits related to the basal ganglia [10]. In this study, we utilized a modified task due to the inability of $CHCHD10^{S55L}$ animals to re-orient to a head-down position from the typical head-up starting position on the pole. During the testing phase, animals were placed head-down on a pole (50 cm × 8 mm diameter). The time from tail release to placement of all four paws on a padded base was recorded for three trials per mouse.

The novel object recognition task is widely used to assess recognition memory [20]. Mice were habituated to the testing chamber for 1 h before they were exposed to two objects for three sessions of 5 min for 3 days. Following each

session, the objects and cage were cleaned with 70% ethanol. Following a retention interval of 24 h after the last training session, mice were exposed to one familiar object and one novel object for 5 min. Behavior was recorded during the entire testing phase and total exploration time and time spent with each object was measured via real-time digital processing of recordings (Any-Maze, Stoelting).

Gross motor activity and anxiety-like behaviors were assessed by placing mice in a novel, open, and well-lit arena (40 cm × 40 cm) monitored by video and were allowed to explore freely for 5 min. Total distance traveled in meters and time in the center section of the field in seconds were recorded (Any-Maze, Stoelting).

Blood was collected by retro-orbital draw and allowed to clot for 2 h at room temperature. Serum was separated at 3000×*g* for 5 min and FGF-21 concentration was assayed according to the manufacturer's instruction (Quantikine ELISA, R & D Systems).

Mice used for pathology studies were euthanized by CO_2 asphyxiation. Organs were fixed in 10% buffered formalin for 48 h before routine processing and embedding in paraffin. Sections were cut at a thickness of 5 µm and stained with hematoxylin and eosin (H&E). Histochemical stains such as Masson's Trichrome and Oil Red O were performed to assess collagen content and presence of cytoplasmic lipid vacuoles in the heart, respectively, on formalin-fixed, snap-frozen and OCT-embedded samples of the heart. Necropsy and histopathology evaluation was performed by a board-certified veterinary pathologist (AP).

Electron microscopy and immunohistochemistry

Mice were terminally anesthetized with sodium pentobarbital (150 mg/kg, i.p.) and perfused intracardially with 2% heparin in normal saline followed by 3.75% acrolein and 2% PFA in phosphate buffer (PB) [27]. Tissues were post-fixed in 2% acrolein and 2% PFA in PB for 30 min. Brain and spinal cord tissue was sectioned at 40 µm on a Vibratome (Leica). Sections used for immuno-electron microscopy and quantitative immunofluorescence were coded by hole punches and followed identical conditions throughout all procedures to ensure equal labeling between groups [27]. Gastrocnemius muscle was dissected and immunostained in small, intact muscle fibers. Sections or tissue were incubated with primary antibody (Supplementary Materials and Methods) for 24 h at room temperature (RT) and 24 h at 4 °C and appropriate secondary antibodies for 2 h at RT. Sections were imaged on a Leica TCS SP5 confocal laser-scanning microscope using identical parameters for WT and experimental sections. Fluorescence intensity was quantified using MetaMorph software (Molecular Devices).

Immunogold labeling of TH+ neurons was performed as previously described [4, 27]. Briefly, after primary antibody incubation (Supplementary Material), sections were incubated overnight in secondary antibody conjugated to 1-nm gold particles (1:50, Electron Microscopy Sciences) and enhanced with a SEKL 15 Silver Enhancement kit (Ted Pella).

Midbrain, spinal cord, heart, and skeletal muscle sections were post-fixed in 2% osmium tetroxide, dehydrated, and flat embedded. Ultrathin sections (70 nm) were cut, collected on copper grids, counterstained with uranyl acetate and Reynold's lead citrate, and imaged on an electron microscope (CM10, FEI). Images were collected and quantified for abnormal mitochondria by an operator blinded to mouse genotype.

Subcellular fractionation, lysis, and Western blotting

Cytosolic and mitochondrial fractions were prepared from fresh heart tissue according to a standard protocol [14].

Tissues used for blotting and filter trap analysis were rapidly dissected from euthanized mice and snap frozen in liquid nitrogen in tissue storage solution (320 mM sucrose, 10 mM Tris, pH 7.2, 20% DMSO). Thawed tissues were washed and homogenized on ice in buffer (320 mM sucrose, 10 mM HEPES pH 7.2, 0.2 mM EDTA, 1 mg/mL fatty acid-free BSA) with 1 × protease and phosphatase inhibitors (Halt™, Thermo Fisher) using a glass/Teflon homogenizer. Debris were spun down at 800×*g* for 10 min and the supernatant containing whole cell homogenates was recovered.

For all samples, protein concentration was determined (Pierce BCA Protein Assay Kit, Thermo Fisher). To separate proteins by electrophoresis, equal amounts were mixed with 4 × Laemmli buffer (Bio-Rad) containing β-mercaptoethanol before loading onto AnyKD™ Mini-PROTEAN® TGD™ precast polyacrylamide gels. Proteins were electro-transferred to PVDF membranes (Bio-Rad) using a Trans-Blot® Turbo™ transfer system (Bio-Rad). Membranes were probed overnight with specific primary antibodies (Supplementary Material). After HRP-conjugated secondary antibody incubation, blots were imaged with enhanced chemiluminescence (Bio-Rad) using a ChemiDoc imaging system (Bio-Rad).

Oxygen consumption

Oxygen consumption was measured in freshly isolated heart mitochondria at 37 °C using polarographic oxygen sensors in a two-chamber Oxygraph (OROBOROS Instruments) as previously described [4]. Oxygen consumption was measured with specific substrates for complex I (2 mM malate, 5 mM glutamate) or complex II (10 mM succinate, 5 mM glutamate) in MS–EGTA buffer (210 mM mannitol, 70 mM

sucrose, 1 mM EGTA, 5 mM HEPES) with 2 mM H_2KPO_4 and 1 mM $MgCl_2$.

Filter trap assay

Insoluble protein aggregates were detected by filter trap assay as previously described [28]. Briefly, 25 µg of total homogenate, cytosolic fraction, or mitochondrial fractions were treated with 0.5% Triton X-100 for 15 min on ice. Samples were loaded onto a Bio-Dot Microfiltration apparatus (Bio-Rad) containing a cellulose acetate membrane (0.2 µm pore diameter, Whatman). Vacuum was applied to pass samples through the membrane, which was then was washed with 0.5% Triton X-100 in PBS. Proteins were detected with specific antibodies.

In silico hydropathy analyses

Kyte–Doolittle hydropathy plots of WT and CHCHD10^{S55L} amino acid sequences were generated with the ProtScale server [12].

RNA-seq analyses

cDNA libraries were generated using the Illumina TruSeq RNA Sample preparation kit and sequenced with single-end 50 bps on a HiSeq 4000 sequencer (Illumina). The raw sequencing reads in BCL format were processed through bcl2fastq 2.19 (Illumina) for FASTQ conversion and demultiplexing. RNA reads were aligned and mapped to the mm9 mouse reference genome by TopHat2 (Version2.0.11) [19], and transcriptome reconstruction was performed by Cufflinks (Version 2.1.1) (http://cole-trapnell-lab.github.io/cufflinks/). The abundance of transcripts was measured with Cufflinks in Fragments Per Kilobase of exon model per Million mapped reads (FPKM) [2, 3, 37, 38]. Gene expression profiles were constructed for differential expression, cluster, and principle component analyses with the DESeq 2 package [24].

Statistical analysis

Data are presented as average ± standard deviation (SD) or standard error of the mean (SEM), as indicated in figure legends. Statistical comparisons were made in GraphPad Prism (GraphPad Software Inc.). As a general rule, two sample comparisons were done by unpaired Student's *t* test. Comparisons among groups of repeated measures were done by ANOVA with repeated measures and Holm–Sidak correction for multiple comparisons. Datasets were tested for normal distribution and were normally distributed unless specified. Kaplan–Meier survival curves were compared using the log-rank test. For differential expression analysis, pairwise comparisons between two or more groups using parametric tests where read-counts follow a negative binomial distribution with a gene-specific dispersion parameter were done. Corrected *p* values were calculated based on the Benjamini–Hochberg method to adjust for multiple testing. Data used as references (e.g., WT controls) were set at 100% or 1.0. p values < 0.05 were considered significant.

Results

CHCHD10^{S55L} mice exhibit motor phenotypes and decreased life span

We employed CRISPR/Cas9 endonuclease-mediated gene editing to generate mice with a knock-in mutation in Chchd10 resulting in an S55L amino acid substitution, which corresponds to the human S59L mutation (Fig. 1a). With the use of appropriate RNA guides and a mutagenic donor DNA oligomer, a C to T mutation was introduced in exon 2 of the mouse gene, which changes the codon for serine into leucine (Fig. 1b, c). While CHCHD10^{S55L} mice were viable and born at Mendelian ratio, both male and female heterozygote CHCHD10^{S55L} mice had a shortened life span [344 ± 6.7 (SEM) days] (Fig. 1d). CHCHD10^{S55L} mice developed a phenotype characterized by severe kyphosis (Fig. 1e) and decreased body weight relative to wild-type littermates (WT), starting approximately at 200 days of age in females (Fig. 1f) and before 125 days in males (Fig. 1g). We also examined a cohort of homozygote CHCHD10^{S55L} mice and found a more severe body weight loss than heterozygote animals (Fig. 1f, g).

WT and CHCHD10^{S55L} mice were monitored for motor performance starting at 125 days of age. Heterozygous CHCHD10^{S55L} mice showed a decline in forelimb grip strength relative to WT, starting at approximately 260 days of age (Fig. 2a). In homozygote CHCHD10^{S55L} mice, the grip strength deficit was more severe than in heterozygous mice and present at the earliest time points tested (Fig. 2a). CHCHD10^{S55L} mice also exhibited exercise intolerance, defined by time spent on an accelerating treadmill, starting at 150 days of age (Fig. 2b). Treadmill performance was more severely impaired in homozygous animals (Fig. 2b). Muscle weakness corresponded to a marked decrease in the muscle mass of CHCHD10^{S55L} mice relative to WT at 330 days of age, which was not observed in age-matched CHCHD10 KO mice (Fig. 2c). These results indicated that CHCHD10^{S55L} mice had decreased life span and suffered from muscle weakness and diminished exercise endurance.

We further tested motor behavior using the pole descent task at 330 days of age and observed a limb incoordination phenotype in all CHCHD10^{S55L} mice, characterized by inability to grasp the pole with the hind limbs during

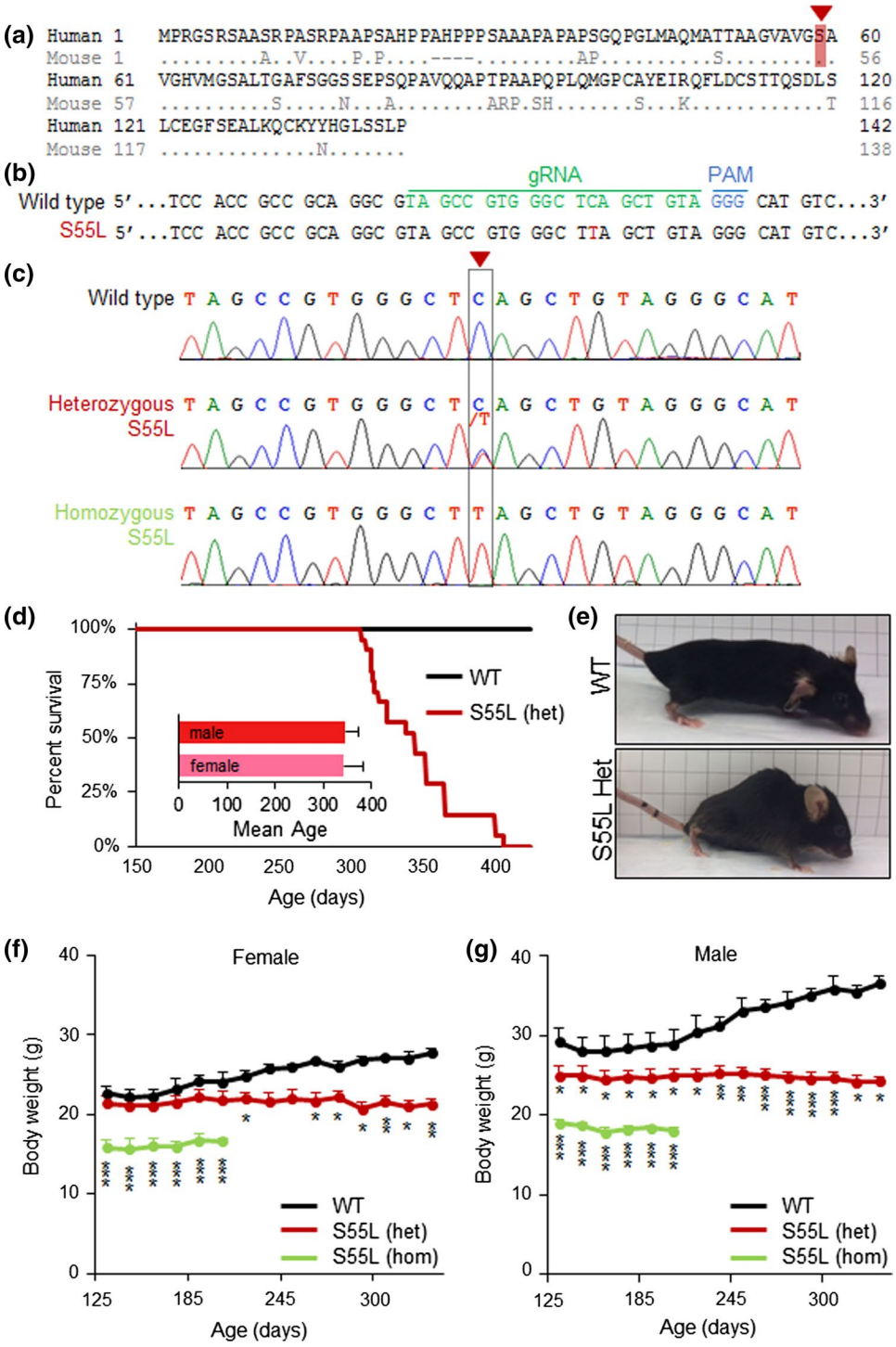

Fig. 1 *Generation of CHCHD10^{S55L} mice*. **a** Alignment of human and mouse CHCHD10 protein sequences. Amino acid S55 in mice corresponds to the S59 in humans (highlighted in red). **b** CRISPR guide RNA to create the TCA→TTA mutation in exon 2 of mouse *CHCHD10* gene which changes the codon for serine to leucine. **c** DNA sequence analyses of heterozygote and homozygote CHCHD10^{S55L} mice. The arrow and dashed box indicate the C→T mutation introduced by gene editing in the *CHCHD10* gene. **d** Kaplan–Meier survival analysis. Heterozygous CHCHD10^{S55L} mice ($n=21$) have shortened lifespan than WT mice ($n=20$). The average lifespan of male ($n=8$) and female ($n=13$) heterozygous CHCHD10^{S55L} mice is shown (inset). **e** Heterozygous CHCHD10^{S55L} mice at 330 days of age show decreased body size and kyphosis. **f**, **g** Body weight measurements. Female and male CHCHD10^{S55L} heterozygote mice exhibit a progressive reduction in average body weight, which is more severe in homozygote CHCHD10^{S55L} mice. $n=5$ mice per group. Error bars indicate SD. $^{*}p<0.05$, $^{**}p<0.01$, $^{***}p<0.001$, by ANOVA with repeated measures and Holm–Sidak correction for multiple comparisons

descent and a clasping of the hind paws or clenching of a single paw (Fig. 2d, Supplementary Movie 1a, b). This defect resulted in a significant delay in pole descent time in CHCHD10^{S55L} mice relative to WT (Fig. 2e). We also observed an abnormal gait in mutant mice characterized by a widened stance and splayed hind limbs (Supplementary Movie 2a, b). These alterations suggested that, in addition to muscle weakness, CHCHD10^{S55L} mice suffered from motor coordination defects. The difference in severity between heterozygote and homozygote CHCHD10^{S55L} mice indicated a clear gene dosage effect. Since in humans the disease manifests in heterozygote individuals, heterozygote CHCHD10^{S55L} mice better reflect the genetics of the disease and the age-related phenotypes. Therefore, for the rest of the study we used exclusively heterozygote CHCHD10^{S55L} mice.

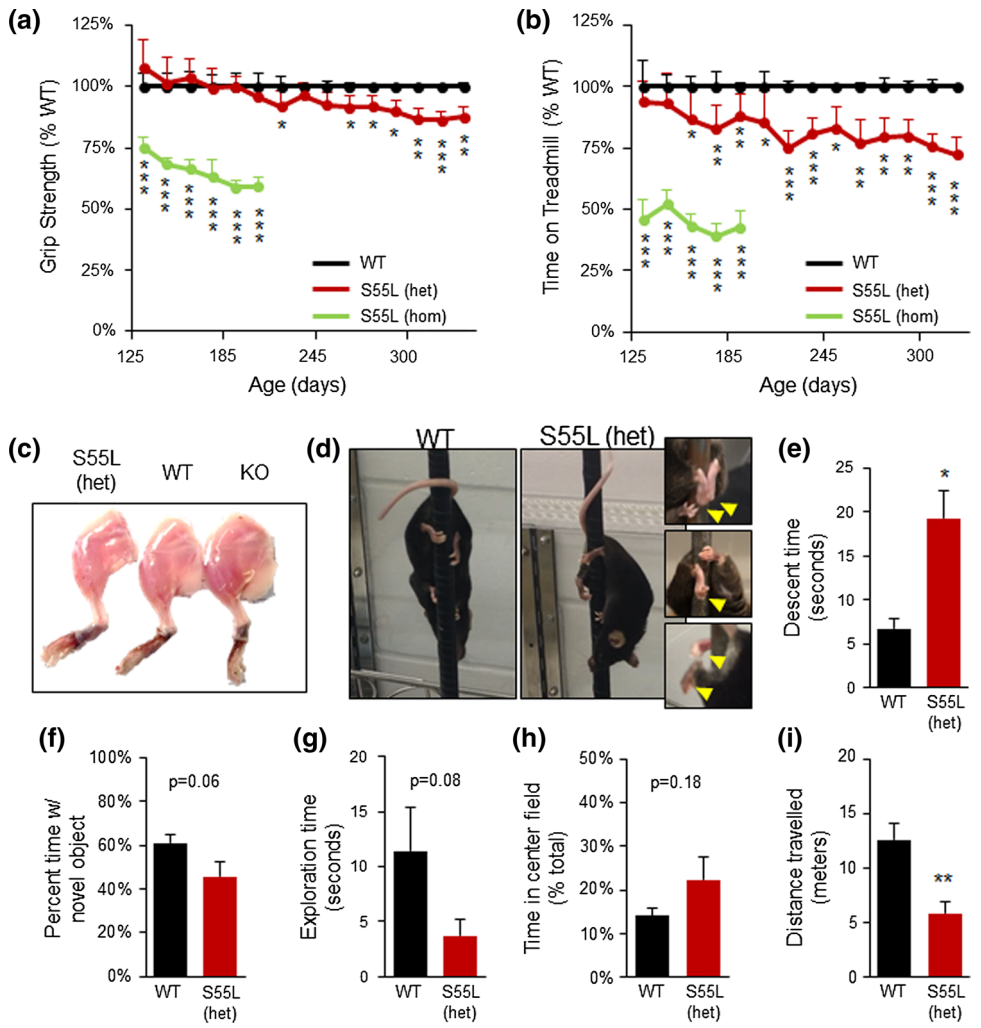

Fig. 2 CHCHD10^{S55L} mice manifest motor symptoms and skeletal muscle atrophy but no cognitive impairment. **a** Forepaw grip strength expressed as percent of WT average. $n=10$ mice per genotype ($n=5$ females, $n=5$ males). Error bars indicate SD. $*p<0.05$, $**p<0.01$, $***p<0.001$ by ANOVA with repeated measures, Holm–Sidak correction for multiple comparisons. **b** Exercise endurance measured by time on the treadmill expressed as percent of WT average. $n=10$ mice per genotype. Error bars indicate SD. $*p<0.05$, $**p<0.01$, $***p<0.001$ by ANOVA with repeated measures, Holm–Sidak correction for multiple comparisons. **c** Image of hind limb musculature of CHCHD10^{S55L} heterozygote, WT, and CHCHD10 KO mice at 330 days of age. **d** Mice on the pole descent task. CHCHD10^{S55L} mice displayed hind limb incoordination characterized by poor hind paw pole grasping (magnified images, arrows). **e** Average pole descent time in mice at 330 days of age. $n=3$ mice per group, 3 trials each mouse. Error bars indicate SEM. $*p<0.05$, by Student's t test. **f**, **g** Novel object recognition test. Average time spent with the novel object and total exploration time recorded during a 5-min testing period in mice at 250 days of age. $n=13$ WT (7 males and 6 females) and $n=16$ CHCHD10^{S55L} mice (8 males and 8 females) mice per group. Error bars indicate SEM. **h**, **i** Open-field test. Average percent time spent in the center field relative to total time, and total distance traveled. $n=13$ WT (7 males, 6 females) and $n=16$ CHCHD10^{S55L} (8 males, 8 females) per group. Error bars indicate SEM. $**p<0.01$ by Student's t test

Because the CHCHD10 S59L mutation has been associated with dementia in humans [1], we sought to test recognition memory functions in CHCHD10^{S55L} mice at 250 days of age, prior to the worsening of the motor phenotype, using the novel object recognition task [20]. CHCHD10^{S55L} mice did not spend significantly less time with the novel object (Fig. 2f), indicating that at this age, recognition memory was preserved. Furthermore, no significant differences were observed in the exploration time (Fig. 2g). In the open-field test, which measures anxiety-like behavior [6], the time spent in the center field by CHCHD10^{S55L} and WT mice did not differ significantly (Fig. 2h), indicating that mutant mice do not have anxiety-like phenotypes. However, CHCHD10^{S55L} mice traveled significantly less during the open-field test (Fig. 2i), suggesting a decrease in spontaneous exploring behavior.

CHCHD10^{S55L} mice develop severe cardiomyopathy and myopathy

Pathology studies of CHCHD10^{S55L} mice at 330 days of age revealed a severe hypertrophic cardiomyopathy (Fig. 3a). Heart weight relative to body weight in mutant animals was increased by 60% relative to WT (Fig. 3b). Hematoxylin and eosin (H&E) staining of heart sections revealed increased wall thickness and narrowing of the ventricular lumen in CHCHD10^{S55L} mice (Fig. 3c). Furthermore, we observed a significantly accelerated mortality of CHCHD10^{S55L} females that became pregnant, compared to naïve (virgin) CHCHD10^{S55L} females (Fig. 3d). This effect was not observed in CHCHD10 KO females, which had normal fertility and lifespan after breeding (data not shown). Postmortem analyses of CHCHD10^{S55L} females mated at 42–56 days revealed a severely dilated heart in CHCHD10^{S55L} breeding females (Fig. 3e), accompanied by fluid-filled thoracic cavities (not shown). Heart failure was reflected in a substantially decreased cardiac ejection fraction and ventricular dilation by echocardiogram (Fig. 3f, g, Supplementary Movie 3a, b). These results reveal a striking cardiomyopathy in CHCHD10^{S55L} mice that is exacerbated in young females by the hemodynamic stress associated with pregnancy.

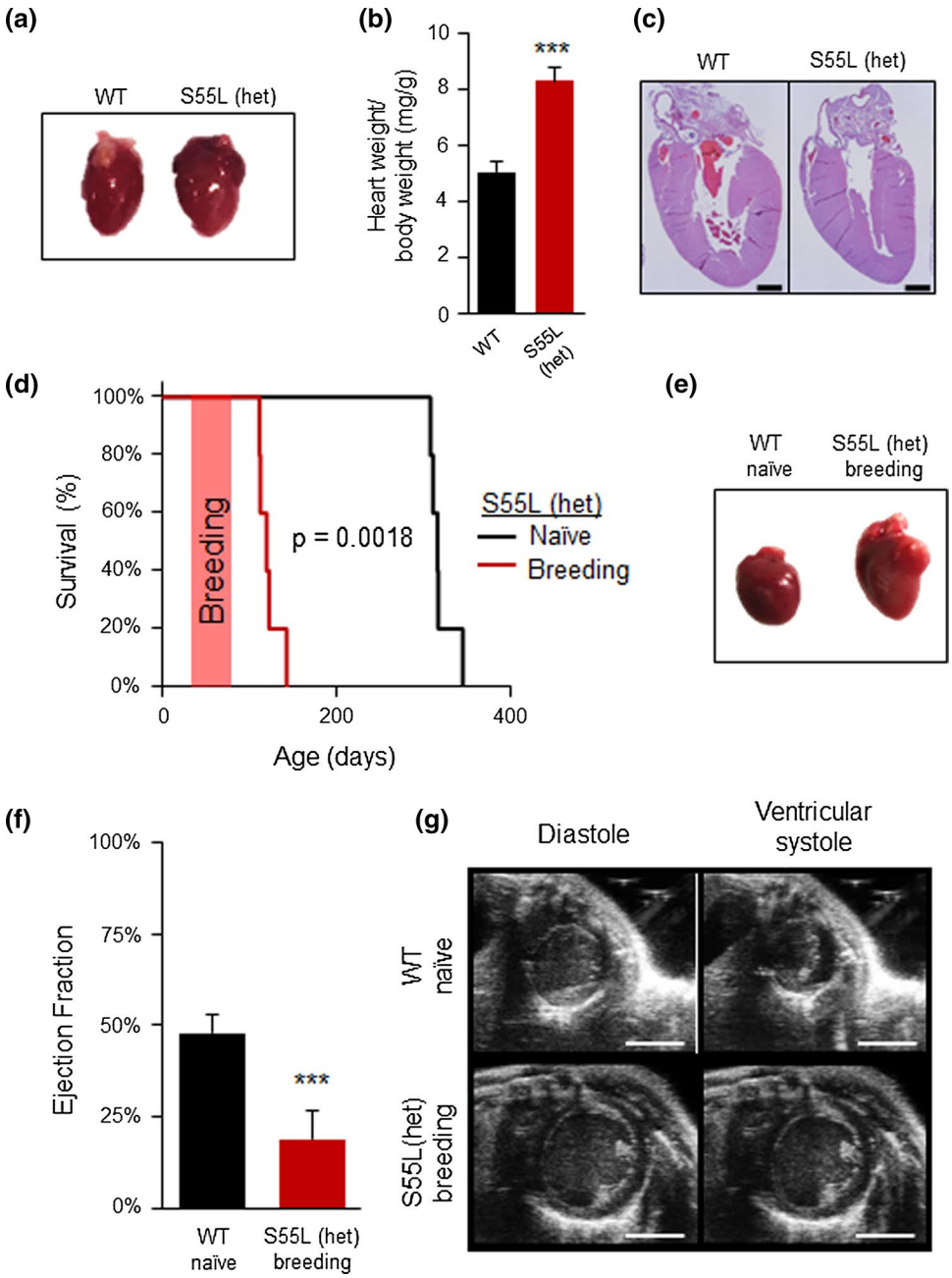

Fig. 3 CHCHD10^{S55L} mice display cardiac hypertrophy exacerbated in breeding females. **a** Hearts at 330 days of age. Cardiac hypertrophy in CHCHD10^{S55L} mice is apparent relative to WT mice. **b** Average heart weight relative to body weight (mg/g). $n=7$ WT (3 males, 4 females) and $n=7$ CHCHD10^{S55L} (3 males, 4 females) mice per group. Error bars indicate SEM. ***$p<0.001$ by Student's t test. **C**. H&E staining of heart sections of WT and CHCHD10^{S55L} mice. Left ventricular wall thickness is increased in CHCHD10^{S55L} heart. Scale bar = 1 mm. **d** Kaplan–Meier survival analysis. CHCHD10^{S55L} breeding females ($n=5$) have shortened lifespan than CHCHD10^{S55L} naïve females ($n=5$). $p=0.0018$ by log-rank test. The orange bar indicates the time when females were breeding. **e** Hearts of WT naïve and CHCHD10^{S55L} breeding females. **f** Left ventricle ejection fraction measured by echocardiogram in WT naïve and CHCHD10^{S55L} breeding female mice at 80–90 days of age. $n=5$. Error bars indicate SEM. ***$p<0.001$ by Student's t test. **g** Images captured from echocardiogram during ventricular diastole and systole. Scale bar = 3 mm

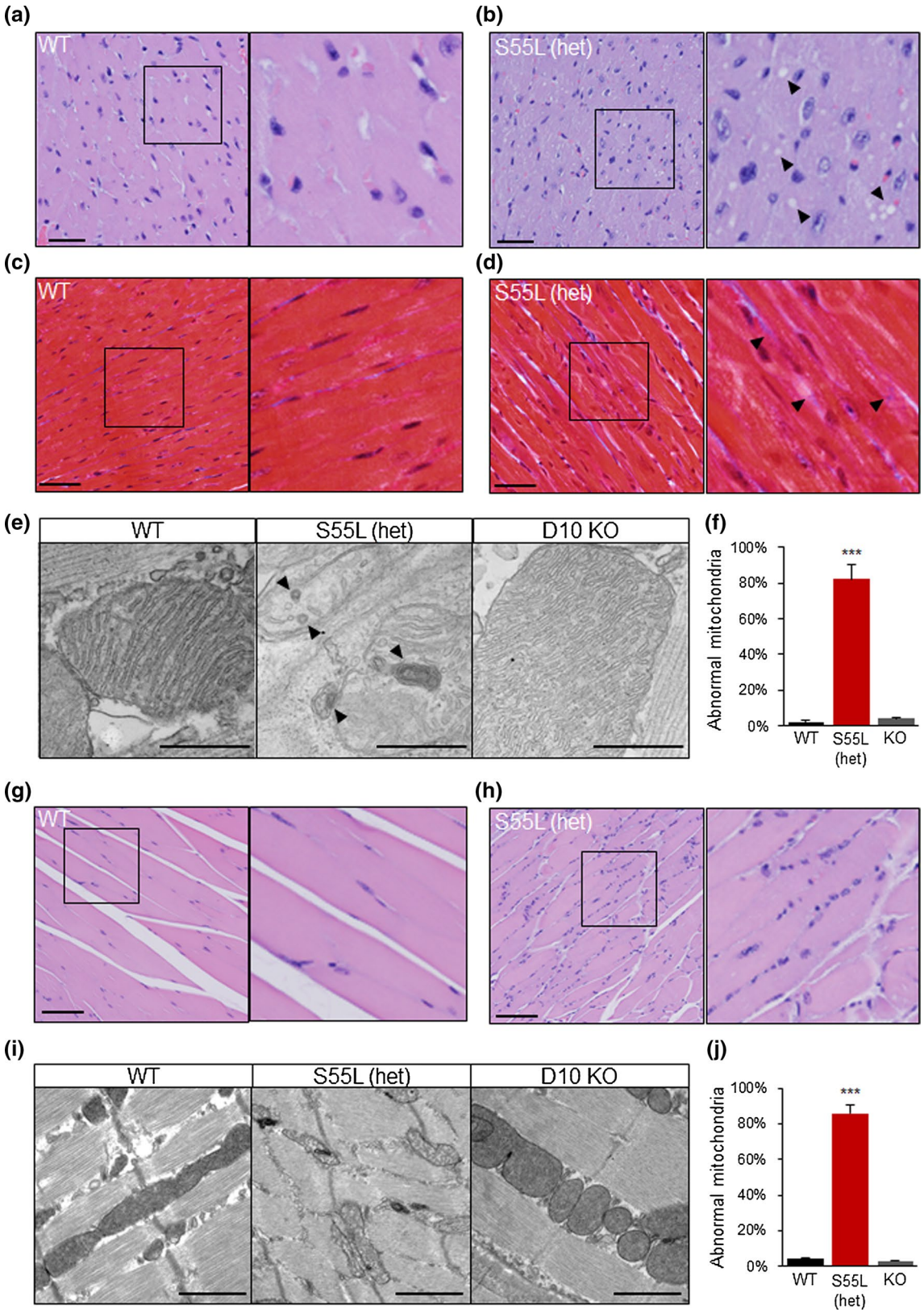
(a)
WT
(b)
S55L (het)
(c)
WT
(d)
S55L (het)
(e)
WT
S55L (het)
D10 KO
(f)
Abnormal mitochondria
100%
80%
60%
40%
20%
0%
***
WT
S55L (het)
KO
(g)
WT
(h)
S55L (het)
(i)
WT
S55L (het)
D10 KO
(j)
Abnormal mitochondria
100%
80%
60%
40%
20%
0%
***
WT
S55L (het)
KO

◂**Fig. 4** Histopathological and ultrastructural abnormalities in CHCHD10^{S55L} muscle and heart. **a**, **b** H&E staining of myocardium in the apical region of hearts from mice at 330 days of age. The right panel of each image is a magnification of the area indicated by the square in the left panel. In **b**, arrows indicate cytoplasmic vacuoles. Scale bar = 50 µm. **c**, **d** Masson's trichrome stain of myocardium of mice at 330 days of age. The right panel of is a magnification of the area indicated by the square in the left panel. In **d**, arrows indicate areas of cardiac interstitium with abundant collagen accumulation. Scale bar = 50 µm. **e** Electron micrographs of mitochondria in WT, CHCHD10^{S55L}, and CHCHD10 KO cardiac tissue. Arrows highlight abnormal membranous structures in mitochondria. Scale bar = 500 nm. **f** Quantification of abnormal heart mitochondria (% of total mitochondria). **g**, **h** H&E staining of quadriceps femoris. The right panel of is a magnification of the area indicated by the square in the left panel. Scale bar = 100 µm. **i** Electron micrographs of WT, CHCHD10^{S55L}, and CHCHD10 KO skeletal muscle. Scale bar = 1 µm. **j** Quantification of abnormal skeletal muscle mitochondria (% of total mitochondria)

The clear disease phenotypes observed in skeletal muscle and heart of CHCHD10^{S55L} mice prompted us to further investigate the histopathology of these tissues. Widespread cytoplasmic vacuolization in cardiomyocytes of both the atria and ventricles was a consistent finding in mutant mice. In H&E-stained sections, vacuoles were well defined, optically empty, and variably sized (Fig. 4a, b). The sharp demarcation of these vacuoles was suggestive of a possible lipid storage, which was excluded with Oil Red O staining (not shown), or an abnormal enlargement of cytoplasmic organelles. Cardiomyocytes in CHCHD10^{S55L} mice also had increased variation of nuclear size compared to WT animals. The cardiac interstitium of CHCHD10^{S55L} heart was more prominent relative to WT when stained by Masson's Trichrome, indicating fibrotic collagen accumulation (Fig. 4c, d). Electron microscopy revealed an increased proportion of mitochondria with profound ultrastructural alterations in CHCHD10^{S55L} heart, characterized by matrix swelling, loss of cristae, and presence of abnormal membranous structures, which were virtually absent in age-matched CHCHD10 KO hearts (Fig. 4e, f).

Myofibers of the gastrocnemius muscle of CHCHD10^{S55L} mice showed a number of myopathic features, including fiber splitting, increased variation of myofiber size with a large number of atrophic and angular fibers, increased nuclear density, and centrally located nuclei (Fig. 4g, h). By electron microscopy, there was a clear disorganization of the sarcomeres, accompanied by an increased number of mitochondria with abnormal ultrastructure, similar to CHCHD10^{S55L} heart mitochondria in CHCHD10^{S55L}, which were virtually absent in CHCHD10 KO, muscle (Fig. 4i, j). Interestingly, all CHCHD10^{S55L} mice analyzed had a sterile otitis media, characterized by effusion and accumulation of macrophages, neutrophils, and degenerating epithelial cells within the tympanic bulla, which could likely be ascribed to the degeneration of the stapedius muscle (Supplementary Fig. 1a, b).

CHCHD10^{S55L} mice manifest neuropathological alterations

Patients affected by the CHCHD10 S59L mutation present with a variety of disorders of the nervous system, including motor neuron degeneration, dementia, and PD. We have previously demonstrated that CHCHD10 is highly expressed in specific cell types of the CNS, including dopaminergic neurons of the midbrain and motor neurons of the spinal cord [4]. We, therefore, sought to determine if CHCHD10^{S55L} mice develop alterations in motor and dopaminergic neurons. We found that 330-day-old WT and CHCHD10^{S55L} mice have comparable numbers of choline acetyl-transferase (ChAT)-positive motor neurons in the anterior horn of the lumbar spinal cord (Fig. 5a, b). However, we detected an increased proportion of mitochondria with abnormal vacuoles in the soma of motor neurons by electron microscopy (Fig. 5c, d), suggesting that CHCHD10^{S55L} motor neuron mitochondria were damaged, but the cell bodies had not yet degenerated.

Degeneration of the neuromuscular junction (NMJ) is an early pathological event in motor neuron disease [9, 25]. Due to the pronounced muscle weakness and muscle fiber atrophy observed, we investigated if CHCHD10^{S55L} NMJs were abnormal. To study NMJ innervation and morphology, we immunostained neuronal terminals in the gastrocnemius muscle for neurofilaments (NF200) and nicotinic acetylcholine receptors (nAChR) with fluorescently labeled alpha-bungarotoxin (BTX). In WT muscle, BTX labeled characteristic pretzel-shaped NMJs innervated by motor neuron terminals (Fig. 5e). Conversely, approximately 50% of NMJs lacked innervation in CHCHD10^{S55L} muscle (Fig. 5e, f). Furthermore, CHCHD10^{S55L} NMJs had abnormal morphology with loss of complexity (Fig. 5g, h) and reduced area (Fig. 5g, i). Abnormal NMJ morphology and innervation is characteristic of ALS [9]. Therefore, these results suggest that a distal motor neuropathy could participate in the muscle weakness and atrophy observed in CHCHD10^{S55L} mice.

Next, we assessed the number of tyrosine hydroxylase-positive (TH+) dopaminergic neurons in the substantia nigra of 330-day-old mice. We observed similar numbers of TH+ cells in CHCHD10^{S55L} and WT substantia nigra (Fig. 6a, b), indicating that there was no overt loss of dopaminergic neurons in mutant animals. However, electron microscopic analyses revealed an increased proportion of abnormal mitochondrial ultrastructure in TH+ neurons in the substantia

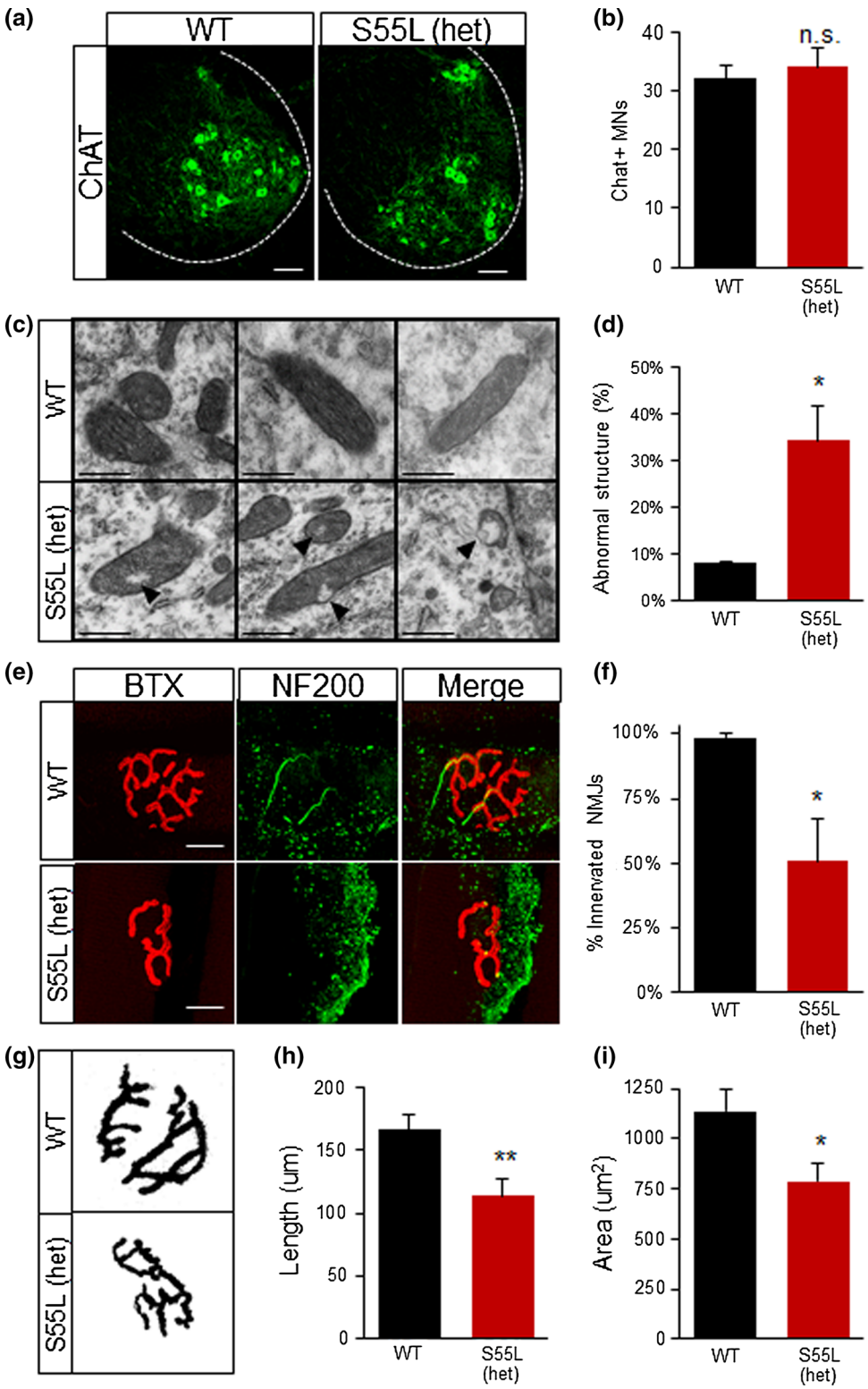

Fig. 5 CHCHD10^{S55L} mice have abnormal neuronal mitochondria and NMJ defects. **a** ChAT immunostaining of motor neurons in lumbar spinal cord. **b** Average number of ChAT+ neurons per lumbar spinal cord section. Bars = 50 µm. $n = 4$, 6 sections per mouse. Error bars indicate SEM. n.s., not significantly different by Student's t test. **c** Electron micrographs of mitochondria in the soma of lumbar spinal cord motor neurons. Arrows indicate intramitochondrial vacuolization in CHCHD10^{S55L} motor neurons. Scale bar = 500 µm. **d** Quantification of abnormal spinal cord motor neuron mitochondria (% of total mitochondria). **e** Gastrocnemius NMJs labeled with TRITC-conjugated BTX (red) and NF-200 (green). Bars = 20 µm. **f** Average numbers of innervated (BTX+ and NF-200+) NMJs in gastrocnemius expressed as a percent of total NMJs imaged. $n = 4$, 10 NMJs per mouse. Error bars indicate SEM. *$p < 0.05$ by Student's t test. **g** Images for morphological analysis of NMJs labeled by BTX taken with fixed settings, and converted to binary images by applying identical thresholds. **h** Average NMJ complexity assessed as the total length of branches in each NMJ. **i** Average area of NMJs. In **h**, **i** $n = 4$ mice per group, 10 NMJs per mouse. Error bars indicate SEM. *$p < 0.05$, **$p < 0.01$ by Student's t test

nigra of CHCHD10^{S55L} mice (Fig. 6c, d). These ultrastructural alterations were specific to TH+ cells, because neighboring TH− cells contained normal mitochondria (Fig. 6c). Thus, CHCHD10^{S55L} caused mitochondrial alterations that could result in dopaminergic defects and contribute to motor dysfunction.

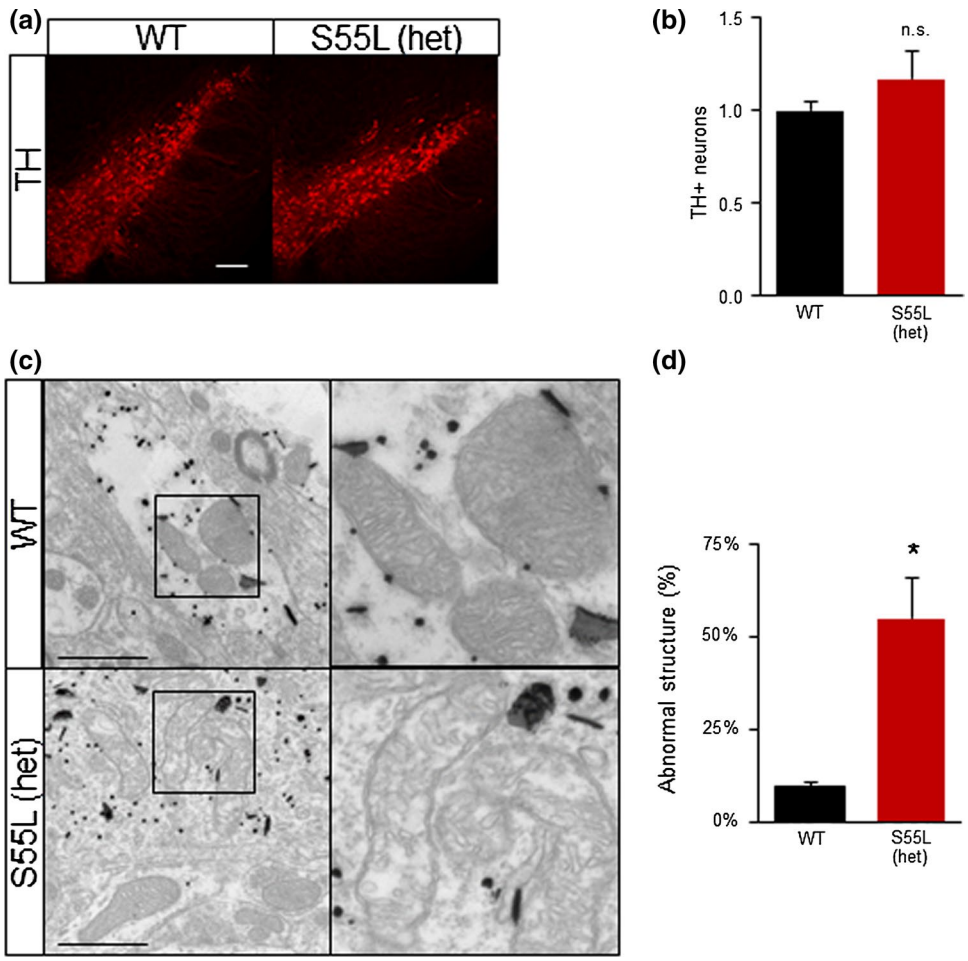

Fig. 6 CHCHD10^{S55L} mice have abnormal mitochondria in dopaminergic neurons. **a** TH immunostaining of substantia nigra pars compacta. Bars = 100 µm. **b** Average TH+ neurons count in a 200 × 500 µm area encompassing the substantia nigra pars compacta expressed relative to WT. $n = 4$ mice, 4 areas per mouse. n.s., not significantly different by Student's t test. **c** Electron micrographs of mitochondria in immunogold labeled TH+ neurons of the substantia nigra. Abnormal cristae and vacuolization are visible in CHCHD10^{S55L} TH+ neurons. The right panel of each image is a magnification of the area indicated by the square in the left panel. Scale bar = 1 µm. **d** Quantification of abnormal mitochondria in TH+ neurons (% of total mitochondria)

CHCHD10^{S55L} and CHCHD2 form large insoluble aggregates in mitochondria of affected tissues

To investigate the molecular mechanisms of pathology caused by CHCHD10^{S55L}, we first assessed CHCHD10 protein content in heart cytosolic and mitochondrial fractions. We observed that in CHCHD10^{S55L} heart there was a striking accumulation of CHCHD10 selectively in mitochondria (Fig. 7a). As expected, CHCHD10 was absent in both fractions of CHCHD10 KO mice. Intriguingly, CHCHD10 was distributed both in cytosolic and mitochondrial fractions of WT hearts. We excluded the possibility that the cytosolic localization of CHCHD10 was due to a loss of mitochondrial outer membrane integrity because the intermembrane protein cytochrome c was only detected in the mitochondrial fractions, albeit severely decreased in CHCHD10^{S55L} relative to WT and CHCHD10 KO. The accumulation of CHCHD10 in mutant heart mitochondria was paralleled by an increase of the paralog protein CHCHD2, while CHCHD10 KO mice did not show significant changes in CHCHD2 content.

CHCHD10 mRNA in CHCHD10^{S55L} heart was unchanged relative to WT (Supplementary Table 1) and CHCHD2 mRNA was significantly decreased (Fig. 7b), while there was no significant change in CHCHD2 mRNA levels in CHCHD10 KO heart. Furthermore, it was previously shown that CHCHD10 and CHCHD2 have short half-lives, in the order of a few hours [4, 15]. Taken together, this evidence clearly indicates that the aberrant accumulation of CHCHD10 and CHCHD2 in mutant heart mitochondria was due to delayed protein turnover rather than increased protein synthesis.

Protein aggregation is a common feature of neurodegenerative disorders [17] and can lead to sequestration and accumulation of proteins in intracellular compartments. To determine if CHCHD10 and CHCHD2 aggregated in CHCHD10^{S55L} heart mitochondria, we utilized a filter trap assay that captures large detergent-insoluble protein aggregates. We detected strong immunoreactivity for both CHCHD10 and CHCHD2 in homogenates of CHCHD10^{S55L} heart, but not in CHCHD10 KO (Fig. 7c). Importantly, these unfilterable aggregates of CHCHD10 and CHCHD2 were largely confined to mitochondrial fractions. We also identified the presence of large CHCHD10 immunoreactive aggregates in CHCHD10^{S55L} heart (Fig. 7d). Therefore, in

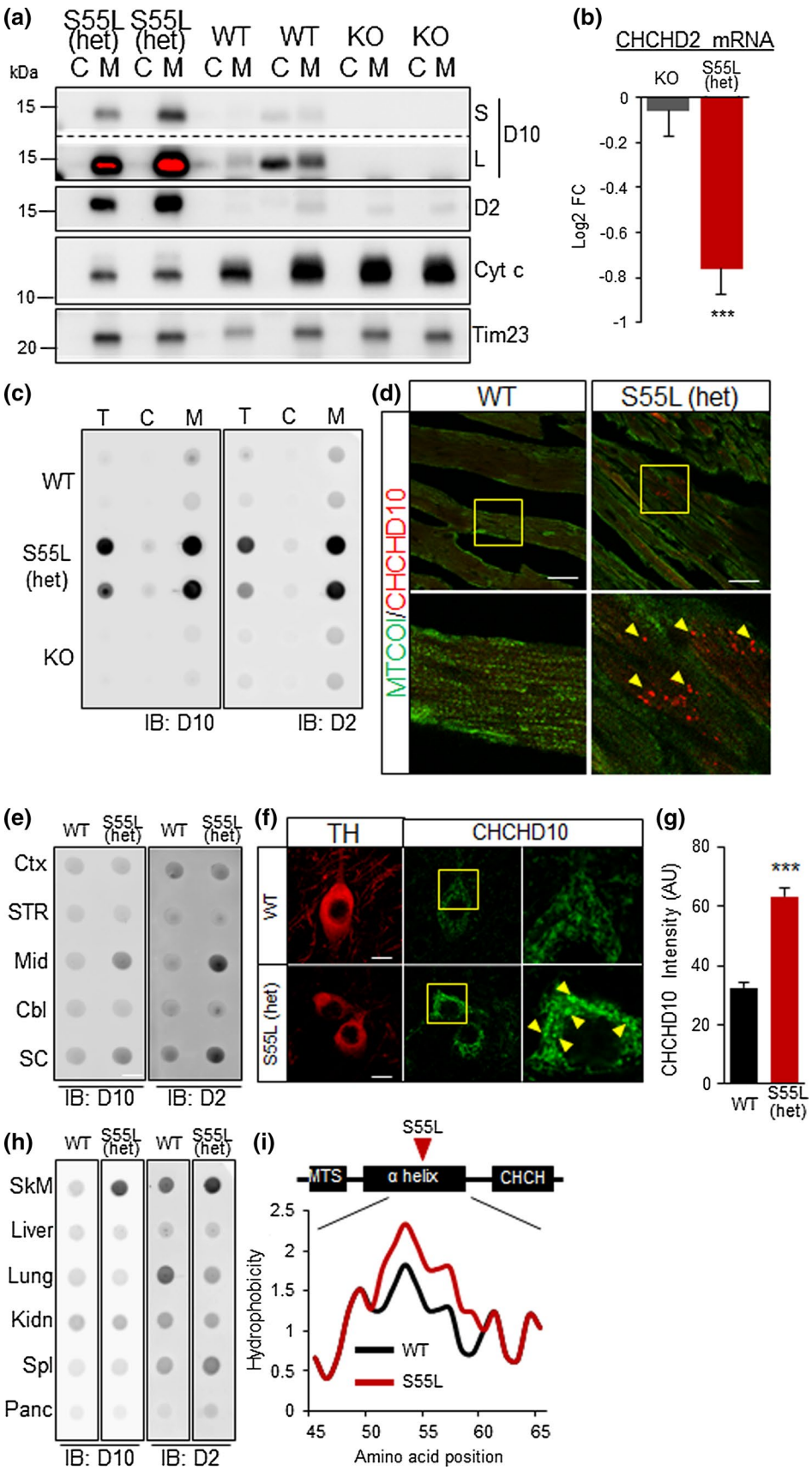
(a)
S55L (het) C M
S55L (het) C M
WT C M
WT C M
KO C M
KO C M
kDa
15
15
15
10
20
S
L
D10
D2
Cyt c
Tim23
(b)
CHCHD2 mRNA
KO
S55L (het)
Log2 FC
0
-0.2
-0.4
-0.6
-0.8
-1
***
(c)
T C M T C M
WT
S55L (het)
KO
IB: D10
IB: D2
(d)
WT
S55L (het)
MTCOI/CHCHD10
(e)
WT S55L (het) WT S55L (het)
Ctx
STR
Mid
Cbl
SC
IB: D10
IB: D2
(f)
TH
CHCHD10
WT
S55L (het)
(g)
CHCHD10 Intensity (AU)
80
60
40
20
0
***
WT
S55L (het)
(h)
WT S55L (het) WT S55L (het)
SkM
Liver
Lung
Kidn
Spl
Panc
IB: D10
IB: D2
(i)
S55L
MTS
α helix
CHCH
Hydrophobicity
2.5
2
1.5
1
0.5
0
WT
S55L
45
50
55
60
65
Amino acid position

◂**Fig. 7** Mutant CHCHD10 aggregates with CHCHD2 in mitochondria of affected tissues. **a** Western blot of heart cytosolic (C) and mitochondrial (M) fractions. D10, CHCHD10; D2, CHCHD2; Cyt c, cytochrome c, short (S) and long (L) exposures are shown for D10. The red color in L indicates overexposure. The inner membrane protein Tim23 was used as a loading control. **b** CHCHD2 mRNA content measured by RNA-seq and expressed as average log2 fold change relative to WT control. Error bars indicate SEM. ***$p < 0.001$ by Student's *t* test with Benjamini–Hochberg correction. **c** Filter trap analysis of total homogenate (T), cytosolic (C) and mitochondrial (M) fractions from heart. Immunoreactive material was detected by immunoblot (IB) with either D10 or D2 antibodies. **d** Cardiomyocytes immunolabeled with antibodies against CHCHD10 (red) and cytochrome oxidase subunit 1 (MTCOI). Bars = 25 µm. The lower panel in each image is a magnification of the area indicated by the square in the top panel. **e** Filter trap analysis of specific brain regions for D10 and D2 aggregates. Immunoreactive material was detected by immunoblot (IB) with either D10 or D2 antibodies. *Mid* midbrain, *SC* spinal cord, *CTX* cortex, *Str* striatum, *Cbl* cerebellum. **f** Substantia nigra neurons immunostained for TH and CHCHD10. Bars = 10 µm. The right panel in each image is a magnification of the area indicated by the square in the middle panel. Hyper-intense CHCHD10-positive puncta are indicated by arrows. **g** Average CHCHD10 immunolabeling intensity in TH+ neurons of the substantia nigra. $n = 20$ WT and $n = 35$ CHCHD10^{S55L} TH+ neurons, from 4 animals per group. Error bars indicate SEM. ***$p < 0.001$ by Student's *t* test. **h** Filter trap analysis of peripheral tissues for D10 and D2. *SkM* skeletal muscle, *Kdn* kidney, *Spl* spleen, *Panc* pancreas. **i** Kyte–Doolittle hydrophobicity plots of the α-helices of CHCHD10 WT and CHCHD10^{S55L}

CHCHD10^{S55L} heart, mitochondrial abnormalities and histopathology are associated with the accumulation of mitochondrial CHCHD10/D2 aggregates.

To determine the relationship between the presence of aggregates and CHCHD10^{S55L} CNS pathology, we performed filter trap assays on tissue from several brain regions (cortex, striatum, midbrain, cerebellum, and spinal cord) and observed increased CHCHD10 and CHCHD2 immunoreactivity only in mitochondria from CHCHD10^{S55L} midbrain and spinal cord (Fig. 7e). In the substantia nigra, we observed that TH+ neurons had stronger CHCHD10 immunoreactivity compared to WT (Fig. 7f, g) and contained large, intensely immunoreactive puncta indicative of protein aggregation. We also assayed peripheral organs other than heart (skeletal muscle, liver, lung, kidney, spleen, and pancreas) by filter trap and found that, in addition to heart, only skeletal muscle presented increased CHCHD10/2 immunoreactivity (Fig. 7h). Overall, the presence of CHCHD10/2 aggregates specifically in affected tissues supports the hypothesis that mitochondrial protein aggregates contribute to pathology, because both gross and histological examination of all the organs and tissues devoid of CHCHD10/2 aggregates in mutant mice did not show morphological abnormalities and the blood chemistry reflected normal liver and kidney function (Supplementary Table 2), despite high protein expression in these tissues [4].

Both CHCHD10 and CHCHD2 contain hydrophobic stretches that could participate in their membrane association or protein–protein interactions. Interestingly, we found that the S55L mutation increased the hydrophobicity of the most hydrophobic portion of the protein, as determined by in silico comparative analysis of the Kyte–Doolittle hydrophobicity plots of WT CHCHD10 and CHCHD10^{S55L} (Fig. 7i). This raises the intriguing possibility that the S55L mutation alters the normal membrane association of the protein, its interaction with other proteins, or its normal intra-mitochondrial distribution to induce aggregation and pathology.

It was previously reported that mutations in CHCHD10 alter the nuclear localization of TAR DNA-binding protein 43 (TDP-43) causing its cytoplasmic redistribution [39]. Therefore, we performed TDP-43 immunocytochemistry of WT and CHCHD10^{S55L} heart sections and found that in WT cardiomyocytes the majority of TDP-43 co-localized with the nuclear stain TOPRO, indicating a mostly nuclear distribution (Fig. 8a). In contrast, large TDP-43 puncta were distributed throughout the cytosol of CHCHD10^{S55L} cardiomyocytes, indicating that CHCHD10^{S55L} induced TDP-43 pathology in heart tissue in vivo. Cytoplasmic TDP-43 inclusions may result from recruitment into stress granules in response to cellular stress [22, 31]. Indeed, TDP-43 puncta co-localized with the stress granule marker TIA-1 in CHCHD10^{S55L} heart (Fig. 8b). We also observed cytosolic TDP-43-positive puncta in TH-positive neurons of the substantia nigra in CHCHD10^{S55L} mice (Fig. 8c), indicating the induction of stress granules similar to the heart. However, we did not detect TDP-43 inclusions in ChAT-positive motor neurons in CHCHD10^{S55L} mice (Fig. 8d). At this disease stage (11 months), mitochondrial alterations appeared to be more severe in cardiomyocytes and TH-positive neurons than in motor neurons, suggesting a correlation between mitochondrial alterations and TDP-43 recruitment in stress granules.

The mitochondrial integrated stress response is strongly induced in CHCHD10^{S55L} mice

The normal function of CHCHD10 remains unknown. Thus, in an attempt to gain a high-level understanding of cellular processes affected by loss of the protein, we performed RNA-seq of heart from CHCHD10 KO and WT mice at 1 year of age. Surprisingly, very few transcripts were significantly altered in CHCHD10 KO mice (Fig. 9a, Supplementary Table 2), further supporting our conclusion that mice can adapt to the lack of CHCHD10.

Next, we compared the transcriptomic profiles of CHCHD10^{S55L} and WT hearts at 1 year of age. CHCHD10^{S55L} heart showed > 1000 significantly altered genes relative to WT (Fig. 9b, Supplementary Table 1). Interestingly, many of the significantly altered genes participate in the mitochondrial unfolded protein response (mtUPR) [26] and, more broadly, the mitochondrial

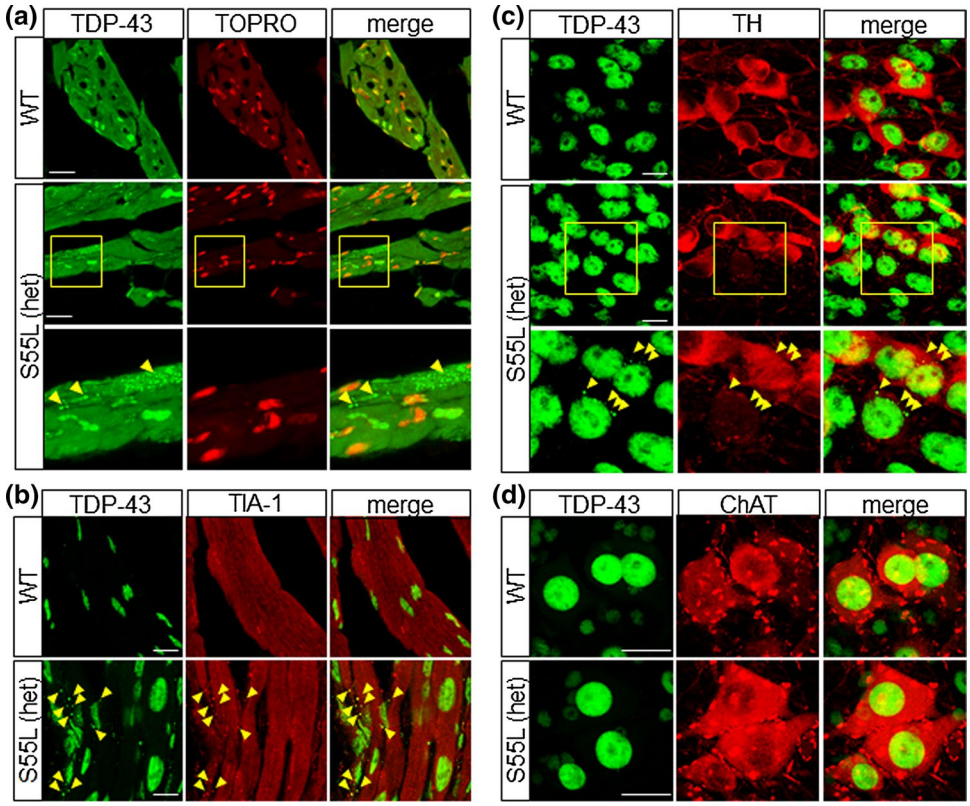

Fig. 8 TDP-43 pathology in mutant CHCHD10 mice. **a** Cardiomyocytes immunolabeled with antibodies against TDP-43 (green) and counterstained with the nuclear probe TOPRO3 (red). The right panels show the merged images. Arrowheads indicate TDP-43 inclusions. **b** Cardiomyocytes immunolabeled with antibodies against TDP-43 (green) and TIA-1 (red). The right panels show the merged images. Arrowheads indicate inclusions positive for both TDP-43 and TIA-1. **c** Midbrain neurons immunolabeled with antibodies against TDP-43 (green) and TH (red). Arrowheads indicate TDP-43 inclusions. **d** Spinal cord motor neurons immunolabeled with antibodies against TDP-43 (green) and ChAT (red). Scale bars = 20 µm

integrated stress response pathway (mtISR), which has been described in mitochondrial myopathies [18]. The stress-induced transcription factor *ATF4* was highly upregulated, as well as many of its validated transcriptional targets, such as *CHOP* and *ATF5* (Fig. 9c). There was also a strong induction of the expression of the two myokines fibroblast growth factor 21 (*Fgf-21*) and growth differentiation factor 15 (*Gdf15*) (Fig. 9c), which were previously shown to be elevated in patients and animal models affected by mitochondrial myopathies [36]. Moreover, expression of genes involved in tetrahydrofolate (THF) biosynthesis for one-carbon metabolism (*Mthfd2*, *Mthfd1L*), serine biosynthesis (*Phgdh*, *Psat1*, *Psph*, *Shmt2*), and glutathione biosynthesis (*Cth*) (Fig. 9d) was markedly elevated (Fig. 9e). Conversely, nuclear-encoded mitochondrial oxidative phosphorylation genes, such as *Cyc1* (cytochrome c) and various subunits of the respiratory chain complexes were repressed (Fig. 9f), as expected in the context of the mtUPR [26].

Increased expression of selected mtISR genes, *Mthfd2*, *Mthfd1L*, and *ATF4*, was confirmed at the protein level by western blot analyses in CHCHD10^{S55L} heart, while there was no change in CHCHD10 KO heart (Fig. 10a). The mtISR was shown to be activated through the mammalian target of rapamycin complex 1 (mTORC1) in mitochondrial myopathy models [18]. Consistent with activation of this pathway, we observed accumulation of the autophagy adaptor p62 in CHCHD10^{S55L} heart by western blot (Fig. 10a) and by immunocytochemistry (Fig. 10b), suggesting stalling of the autophagy process. Co-labeling of the mitochondrial outer membrane protein Tom20 showed partial co-localization with p62, suggesting that p62 is not exclusively accumulating on mitochondria (Fig. 10b). As a further confirmation that mTORC1 was activated in CHCHD10^{S55L} heart, we found a strong increase in the phosphorylation of the ribosomal protein S6, which is phosphorylated downstream of mTORC1, relative to total S6 (Fig. 10a).

Since activation of the mtISR induced a decline in the expression of mitochondrial oxidative phosphorylation genes, we measured mitochondrial respiration by oxygraphy in enriched mitochondrial fractions obtained from the hearts of 330-day-old mice. CHCHD10^{S55L} heart mitochondria had significantly decreased respiration relative to WT with substrates for both complex I (malate/glutamate) and complex II (succinate/glutamate) (Fig. 10c). Therefore, it is plausible that mitochondrial damage caused by aggregation of CHCHD10/2 triggers the mtISR and the downregulation of oxidative phosphorylation gene expression, which further impairs mitochondrial respiratory function.

mtISR induced expression of *Fgf-21*, which is a myokine secreted by muscle into the bloodstream. Fgf-21 has profound effects on the metabolism of distal tissues, notably liver and adipose tissue. We measured serum Fgf-21 levels at different ages and found that it was already significantly elevated in CHCHD10^{S55L} mice relative to WT at 180 days,

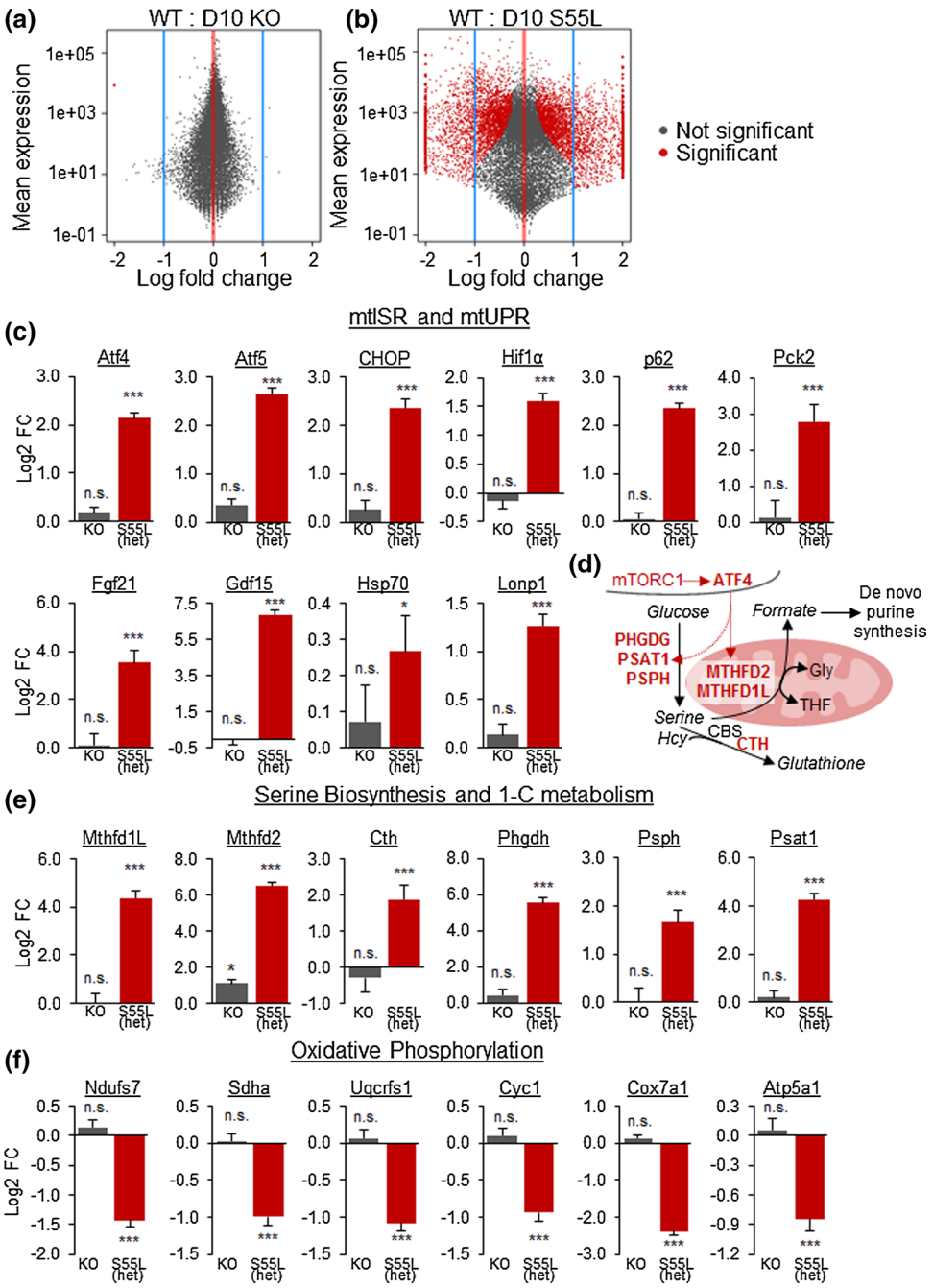

Fig. 9 CHCHD10^{S55L} hearts activate a transcriptional profile of mtISR. **a**, **b** Volcano plots of transcriptomic changes in CHCHD10 KO and CHCHD10^{S55L} hearts relative to WT heart. **c** Changes (log2 fold) in heart RNA content of genes involved in mtUPR and mtISR. *Hif1α* hypoxia-induced factor 1α, *Pck2* phosphoenolpyruvate carboxykinase 2, *Hsp70* heat shock protein 70, *Lonp1* Lon protease homolog, *n.s.* not significant. *$p < 0.05$, ***$p < 0.001$, by Student's *t* test with Benjamini–Hochberg correction. **d** Schematic diagram of enzymes involved in serine biosynthesis and one-carbon metabolism under ATF4 transcriptional regulation. *PHGDH* phosphoglycerate dehydrogenase, *PSAT1* phosphoserine aminotransferase 1, *PSPH* phosphoserine phosphatase, *MTHFD2* methylenetetrahydrofolate dehydrogenase 2, *MTHFD1L* methylenetetrahydrofolate dehydrogenase 1-like, *CTH* cystathionine gamma-lyase. **e** Changes (log2 fold) in heart RNA content of genes involved in serine biosynthesis and one-carbon metabolism. ***$p < 0.001$, by Student's *t* test with Benjamini–Hochberg correction. **f** Changes (log2 fold) in heart RNA content of genes encoding subunits of the mitochondrial oxidative phosphorylation complex I (Ndufs7), II (Sdha), III (Uqcrfs1), IV (Cox7a1), and V (Atp5a1) and cytochrome c (cyc1). ***$p < 0.001$, by Student's *t* test with Benjamini–Hochberg correction

when disease symptoms manifest, and remained elevated throughout disease progression. Conversely, CHCHD10 KO mice did not show increased serum Fgf-21 at any age tested (Fig. 10d). Consistent with Fgf-21 elevation and its role in modulating white adipose tissue metabolism by increasing insulin sensitivity [2], we found that the white fat tissue of CHCHD10^{S55L} mice at end stage (380 days) was almost entirely lost, unlike CHCHD10 KO mice, where the amount of fat was similar to WT mice (Fig. 10e).

Taken together, these results demonstrate a chronic induction of the mtISR triggered by mTORC1 activation and ATF4 signaling in CHCHD10^{S55L} mice but not in CHCHD10 KO animals. Chronic mtISR results in profound alterations of metabolism in affected tissues and in non-cell autonomous metabolic effects in peripheral tissues through secretion of myokines.

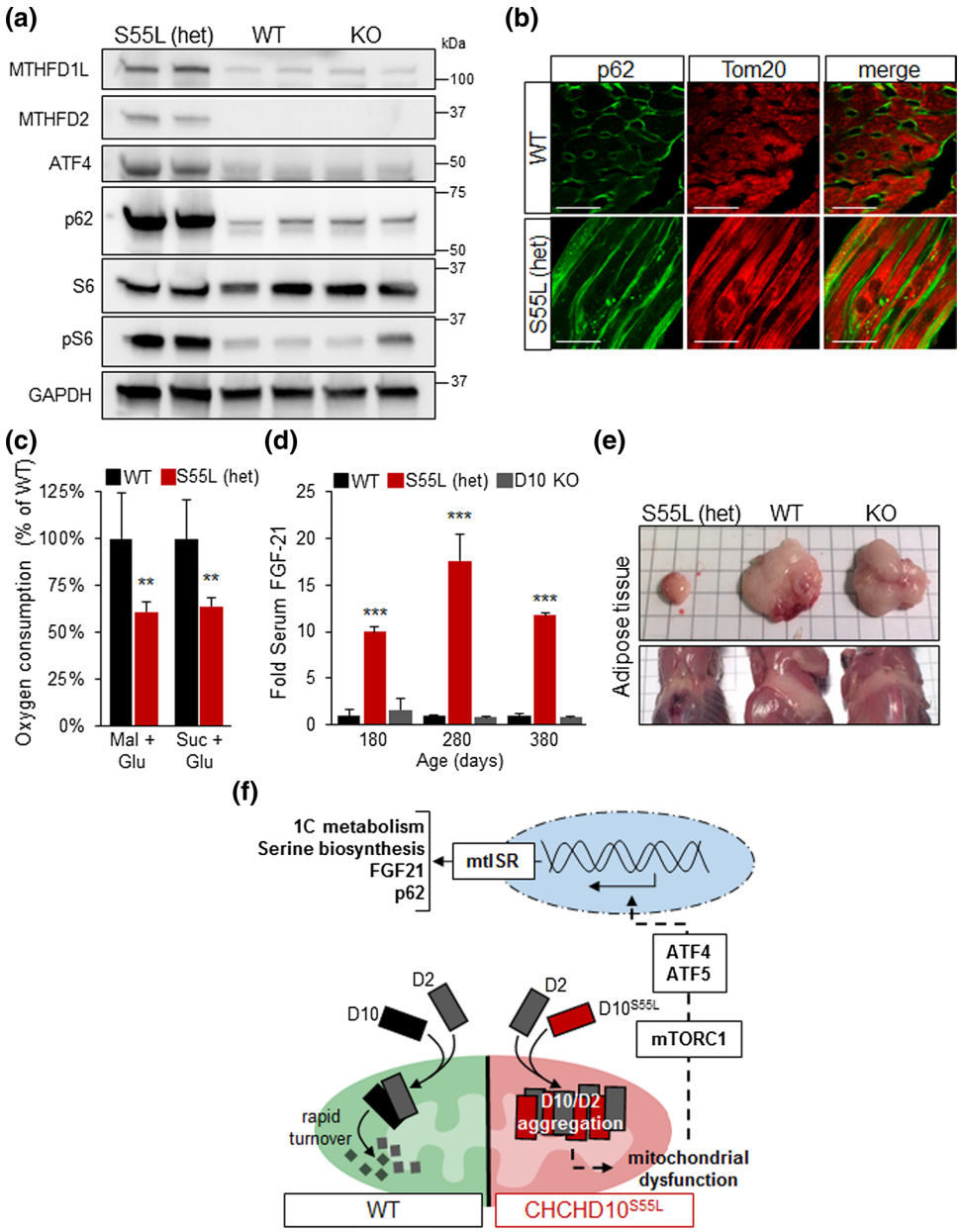

Fig. 10 mtISR leads to mitochondrial dysfunction and systemic metabolic remodeling in CHCHD10^{S55L} mice. **a** Western blots of total heart homogenates for MTHFD1L, MTHFD2, ATF4, p62, phospho-S6, total S6. Glyceraldehyde 3-phosphate dehydrogenase (GAPDH) is used as a loading control. **b** Cardiomyocyte immunolabeling for p62 (green) and Tom20 (red). The right panels show the merged images. Bars = 20 µm. **c** Average oxygen consumption rates in freshly isolated heart mitochondria measured with complex I (glutamate/malate) and complex II (glutamate/succinate) substrates and expressed as a percentage of WT. $n = 6$. Error bars indicate SEM. $^{**}p < 0.01$ by Students t test. **D**. Average FGF-21 levels in mouse serum at 180 days ($n = 10$ WT, 6 CHCHD10^{S55L}, 4 KO), 280 days ($n = 2$ WT, 6 CHCHD10^{S55L}, 2 KO), and 380 days ($n = 8$ WT, 4 CHCHD10^{S55L}, 2 KO) expressed relative to WT. Error bars indicate SEM. $^{***}p < 0.001$ by Student's t test. **e** Visceral (top panel) and subcutaneous (lower panel) fat pads at necropsy. **f** Schematic representation of the pathway of mTORC1/ATF4-mediated mtISR triggered by CHCHD10/2 aggregation and mitochondrial dysfunction in CHCHD10^{S55L} mice

Discussion

Here, we report a novel mutant *CHCHD10* knock-in mouse model that recapitulates several fundamental clinical aspects of human CHCHD10-related mitochondrial diseases. In this mouse model, the mutant protein is under the control of the endogenous promoter, preserving its physiological expression pattern. The CHCHD10 protein sequence is well conserved between humans and mice, except for a stretch of four amino acids missing in the unstructured domain of the mouse protein. Therefore, the highly conserved serine at position 59 in humans corresponds to mouse serine 55. In patients, the CHCHD10 S59L mutation causes a variety of disease phenotypes including ALS, FTD, PD, cardiomyopathy and mitochondrial myopathy [11, 29]. This broad range of phenotypes is not uncommon in primary mitochondrial diseases, as many organs and tissues, especially the most energy-demanding ones, suffer from the consequences of mitochondrial dysfunction [8]. However, *CHCHD10* mutations are unique among mitochondrial disorders because they cause late-onset diseases that are very similar to common neurodegenerative diseases. Hence, CHCHD10 mutants bridge the gap between mitochondrial disorders and neurodegenerative diseases.

CHCHD10^{S55L} mice manifest a late-onset phenotype indicative of neuromuscular dysfunction, which is one of the cardinal features of human CHCHD10-related diseases. We find degeneration of the NMJ, in the absence of spinal

cord motor neuron loss, suggesting that mitochondrial defects lead to distal motor neuropathy. Furthermore, in the midbrain we observe abnormalities of mitochondrial ultrastructure in dopaminergic neurons. Despite the lack of overt cell loss, mitochondrial alterations can cause dysfunction of these neurons resulting in motor incoordination, decline of spontaneous motility, and abnormal gait.

Although a subset of patients with the CHCHD10 S59L mutation suffer from symptoms of dementia, we do not detect obvious cognitive defects in CHCHD10^{S55L} mice at the time when they started developing motor dysfunction (250 days of age). At this point, we cannot exclude that cognitive impairment may arise later in the disease course. However, it must be noted that tests of cognitive function in mice rely on unimpaired mobility. Thus, cognitive phenotypes could be obscured by the neuromuscular defects and loss of motor initiative in CHCHD10^{S55L} at late disease stages.

Previous work exploring the role of CHCHD10 has used patient fibroblasts [13, 35], cell lines overexpressing CHCHD10 [4, 15, 30], or non-mammalian models with transgenic overexpression of the protein [3, 39]. These studies have provided valuable information on the biology of CHCHD10 and CHCHD2, including intracellular localization, trafficking, turnover, and protein–protein interactions but have also led to divergent conclusions about the pathophysiology of CHCHD10 mutations. Our findings comparing the CHCHD10^{S55L} mouse to the CHCHD10 KO mouse provide, for the first time in a mammalian in vivo system, evidence of toxic gain-of-function mechanisms of CHCHD10^{S55L}. Nevertheless, our results cannot exclude that, in humans, loss of CHCHD10 function or a dominant negative function of mutant CHCHD10 could result in mitochondrial dysfunction, over a prolonged period of time.

CHCHD10 and CHCHD2 expression is highly variable in different mammalian cell types [1, 4]. We show that disease phenotypes arise in a subset of tissues that express high amounts of the mutant protein, such as heart, muscle, midbrain dopaminergic neurons, and spinal motor neurons but not in others that also express high levels of the proteins like kidney, liver, and pancreas. We propose that mitochondrial degeneration and disease are linked to the aggregation of mutant CHCHD10/2, and that only the high-expressing cell types in which the proteins aggregate are affected. Future work will investigate the mechanisms underlying the tissue specificity of CHCHD10/2 mitochondrial aggregation, but potential explanations could include differences in the mitochondrial proteostatic systems, such as the levels of chaperones and proteases, or the rate of turnover of mitochondria by autophagy. Intriguingly, cellular stress in the heart induces cytosolic aggregation of TDP-43 and TIA-1, which is a common pathological feature in the CNS of most forms of ALS/FTD [23] and is also found in inclusion body myopathy [7], but never before reported in mitochondrial diseases. Recent studies have demonstrated that activation of the mTOR-S6 kinase pathway promotes stress granule formation [33]. Therefore, we propose that cellular stress initiating in the mitochondria, downstream of CHCHD10/2 aggregation, triggers mTOR-dependent cytosolic mislocalization and aggregation of TDP-43 in CHCHD10^{S55L} mice.

The mechanisms whereby CHCHD10/2 aggregates cause mitochondrial damage and dysfunction may involve sequestration of the two proteins together with other CX_9C proteins essential for mitochondrial homeostasis. A candidate is the mitochondrial disulfide relay protein import system Mia40, on which CHCHD10 mitochondrial import depends [5]. Interestingly, it has been shown that a number of CHCHD10 mutants that harbor mutations in the hydrophobic domain, including S59L, are imported efficiently into mitochondria by Mia40, where they form abnormal clusters [21]. Our results show that mitochondrial protein aggregation triggers a potent mtUPR that results in mTORC1-mediated mtISR. This response involves a number of metabolic pathways, most notably the upregulation of one-carbon and serine metabolism, and global downregulation of nuclear-encoded components of the oxidative phosphorylation machinery (Fig. 10f).

The mtISR has been proposed to be a double edge sword [26]. The accumulation of misfolded proteins in mitochondria is being increasingly recognized as a fundamental pathogenic event in mitochondrial disorders. Protein misfolding and aggregation lead to defective mitochondrial protein import and structural and functional failure of the organelle. As a consequence, mtISR is activated and signals to the nucleus to decrease transcription of mitochondrial genes and upregulate antioxidants and chaperones [32]. In the short term, adaptive mtISR is protective and subsides after transient mitochondrial insults. However, chronic mtISR may be detrimental, ultimately resulting in cellular and organ failure. Maladaptive, prolonged induction of mtISR has been demonstrated in the skeletal muscle of the Twinkle KO mouse model of mitochondrial DNA depletion, where mtISR is activated in an mTORC1-dependent manner [18]. Chronic treatment with rapamycin to inhibit mTORC1 resulted in a striking improvement of the biochemical phenotype and the metabolic alterations, including normalization of the mtISR markers in the Twinkle KO mouse. Rapamycin was also beneficial in other murine models of mitochondrial diseases including the NDUFS4 KO [16] mouse model of Leigh syndrome and the TK2 mutant mouse model of mitochondrial DNA depletion [34], further highlighting the noxious effects of chronic mTORC1-mediated mtISR.

Collectively, our results obtained in the CHCHD10^{S55L} mouse model of mitochondrial disease reveal that aggregation of mutant CHCHD10 in mitochondria causes a tissue-specific toxic gain of function that induces chronic,

maladaptive mtISR. In a back-to-back manuscript in this issue, Genin et. al. report a very similar phenotype in knock-in mice with the same CHCHD10 mutation. The two manuscripts illustrate complementary aspects of CHCHD10^{S55L} mice, including cardiomyopathy and central nervous system involvement, mitochondrial dysfunction, mitochondrial DNA abnormalities, and aberrant cellular responses to metabolic stress. These mouse models will be crucial for testing therapeutic strategies to modulate the mtISR and ameliorate the disease phenotypes. Importantly, while CHCHD10 mutations are relatively rare in the general population, the disease mechanisms identified here can apply to a diverse group of diseases mediated by mtISR dysregulation.

Acknowledgements We acknowledge the funding support of Muscular Dystrophy Association Grant MDA382033 (to G. M.) for this project. We also acknowledge The Jackson Laboratory Genome Engineering Technology and Physiology cores. Costs were defrayed by Cancer Center Support, National Cancer Institute (Grant CA034196) to The Jackson Laboratory. Additional studies were supported using Grant NIH Precision Genetics U54 OD020351 (to C. L.) and NIH/NINDS R01NS062055 (to G. M.). We also acknowledge the WCMC's Center of Comparative Medicine and Pathology, the Neuroanatomy EM Core in the BMRI, and the EM Imaging Core of WCM.

Author contributions GM and CL conceived the study. GM, CL, CJA, AP, TAM, HK, and SRB contributed to experimental design. CL, AZ, CD, and LC designed and performed gene editing and mouse phenotyping. CJA, KB, and SRB performed behavioral experiments. CD and LC performed echocardiography experiments. CJA, TAM, AP, and KB performed histology and electron microscopy experiments. CJA, KB, HK, JD, and SM performed immunohistochemistry and biochemical experiments. GM and CJA analyzed data and drafted the manuscript with input from other authors.

Compliance with ethical standards

Conflict of interest The authors declare no competing interests.

References

1. Bannwarth S, Ait-El-Mkadem S, Chaussenot A, Genin EC, Lacas-Gervais S, Fragaki K et al (2014) A mitochondrial origin for frontotemporal dementia and amyotrophic lateral sclerosis through CHCHD10 involvement. Brain 137:2329–2345. https://doi.org/10.1093/brain/awu138
2. BonDurant LD, Ameka M, Naber MC, Markan KR, Idiga SO, Acevedo MR et al (2017) FGF21 regulates metabolism through adipose-dependent and -independent mechanisms. Cell Metab 25(935–944):e934. https://doi.org/10.1016/j.cmet.2017.03.005
3. Brockmann SJ, Freischmidt A, Oeckl P, Muller K, Ponna SK, Helferich AM et al (2018) CHCHD10 mutations p. R15L and p.G66 V cause motoneuron disease by haploinsufficiency. Hum Mol Genet 27:706–715. https://doi.org/10.1093/hmg/ddx436
4. Burstein SR, Valsecchi F, Kawamata H, Bourens M, Zeng R, Zuberi A et al (2018) In vitro and in vivo studies of the ALS-FTLD protein CHCHD10 reveal novel mitochondrial topology and protein interactions. Hum Mol Genet 27:160–177. https://doi.org/10.1093/hmg/ddx397
5. Cavallaro G (2010) Genome-wide analysis of eukaryotic twin CX9C proteins. Mol BioSyst 6:2459–2470. https://doi.org/10.1039/c0mb00058b
6. Crawley JN (1999) Behavioral phenotyping of transgenic and knockout mice: experimental design and evaluation of general health, sensory functions, motor abilities, and specific behavioral tests. Brain Res 835:18–26
7. Custer SK, Neumann M, Lu H, Wright AC, Taylor JP (2010) Transgenic mice expressing mutant forms VCP/p97 recapitulate the full spectrum of IBMPFD including degeneration in muscle, brain and bone. Hum Mol Genet 19:1741–1755. https://doi.org/10.1093/hmg/ddq050ddq050
8. DiMauro S, Schon EA (2003) Mitochondrial respiratory-chain diseases. N Engl J Med 348:2656–2668
9. Fischer LR, Culver DG, Tennant P, Davis AA, Wang M, Castellano-Sanchez A et al (2004) Amyotrophic lateral sclerosis is a distal axonopathy: evidence in mice and man. Exp Neurol 185:232–240
10. Fleming SM, Salcedo J, Fernagut PO, Rockenstein E, Masliah E, Levine MS et al (2004) Early and progressive sensorimotor anomalies in mice overexpressing wild-type human alpha-synuclein. J Neurosci 24:9434–9440. https://doi.org/10.1523/JNEUROSCI.3080-04.2004
11. Fratter CDE, Carver J, Sergeant K, Barbosa IA, Hofer M, Esiri M et al (2017) Mitochondrial disease and lipid storage myopathy due to mutation in CHCHD10 or DNM1L and disordered mitochondrial dynamics. Neuromusc Disord 27S1:S21
12. Gasteiger E, Gattiker A, Hoogland C, Ivanyi I, Appel RD, Bairoch A (2003) ExPASy: the proteomics server for in-depth protein knowledge and analysis. Nucleic Acids Res 31:3784–3788
13. Genin EC, Plutino M, Bannwarth S, Villa E, Cisneros-Barroso E, Roy M et al (2016) CHCHD10 mutations promote loss of mitochondrial cristae junctions with impaired mitochondrial genome maintenance and inhibition of apoptosis. EMBO Mol Med 8:58–72. https://doi.org/10.15252/emmm.201505496
14. Gostimskaya I, Galkin A (2010) Preparation of highly coupled rat heart mitochondria. J Vis Exp. https://doi.org/10.3791/2202
15. Huang X, Wu BP, Nguyen D, Liu YT, Marani M, Hench J et al (2018) CHCHD2 accumulates in distressed mitochondria and facilitates oligomerization of CHCHD10. Hum Mol Genet. https://doi.org/10.1093/hmg/ddy270
16. Johnson SC, Yanos ME, Kayser EB, Quintana A, Sangesland M, Castanza A et al (2013) mTOR inhibition alleviates mitochondrial disease in a mouse model of Leigh syndrome. Science 342:1524–1528. https://doi.org/10.1126/science.1244360
17. Kawamata H, Manfredi G (2017) Proteinopathies and OXPHOS dysfunction in neurodegenerative diseases. J Cell Biol 216:3917–3929. https://doi.org/10.1083/jcb.201709172
18. Khan NA, Nikkanen J, Yatsuga S, Jackson C, Wang L, Pradhan S et al (2017) mTORC1 regulates mitochondrial integrated stress response and mitochondrial myopathy progression. Cell Metab 26(419–428):e415. https://doi.org/10.1016/j.cmet.2017.07.007
19. Kim D, Pertea G, Trapnell C, Pimentel H, Kelley R, Salzberg SL (2013) TopHat2: accurate alignment of transcriptomes in the presence of insertions, deletions and gene fusions. Genome Biol 14:R36. https://doi.org/10.1186/gb-2013-14-4-r36
20. Leger M, Quiedeville A, Bouet V, Haelewyn B, Boulouard M, Schumann-Bard P et al (2013) Object recognition test in mice. Nat Protoc 8:2531–2537. https://doi.org/10.1038/nprot.2013.155
21. Lehmer C, Schludi MH, Ransom L, Greiling J, Junghanel M, Exner N et al (2018) A novel CHCHD10 mutation implicates a Mia40-dependent mitochondrial import deficit in ALS. EMBO Mol Med. https://doi.org/10.15252/emmm.201708558

22. Li YR, King OD, Shorter J, Gitler AD (2013) Stress granules as crucibles of ALS pathogenesis. J Cell Biol 201:361–372. https://doi.org/10.1083/jcb.201302044
23. Ling SC, Polymenidou M, Cleveland DW (2013) Converging mechanisms in ALS and FTD: disrupted RNA and protein homeostasis. Neuron 79:416–438. https://doi.org/10.1016/j.neuron.2013.07.033
24. Love MI, Huber W, Anders S (2014) Moderated estimation of fold change and dispersion for RNA-seq data with DESeq2. Genome Biol 15:550. https://doi.org/10.1186/s13059-014-0550-8
25. Martineau E, Di Polo A, Vande Velde C, Robitaille R (2018) Dynamic neuromuscular remodeling precedes motor-unit loss in a mouse model of ALS. Elife. https://doi.org/10.7554/elife.41973
26. Melber A, Haynes CM (2018) UPR(mt) regulation and output: a stress response mediated by mitochondrial–nuclear communication. Cell Res 28:281–295. https://doi.org/10.1038/cr.2018.16
27. Milner TA, Waters EM, Robinson DC, Pierce JP (2011) Degenerating processes identified by electron microscopic immunocytochemical methods. Methods Mol Biol 793:23–59. https://doi.org/10.1007/978-1-61779-328-8_3
28. Palomo GM, Granatiero V, Kawamata H, Konrad C, Kim M, Arreguin AJ et al (2018) Parkin is a disease modifier in the mutant SOD1 mouse model of ALS. EMBO Mol Med. https://doi.org/10.15252/emmm.201808888
29. Perrone F, Nguyen HP, Van Mossevelde S, Moisse M, Sieben A, Santens P et al (2017) Investigating the role of ALS genes CHCHD10 and TUBA4A in Belgian FTD-ALS spectrum patients. Neurobiol Aging 51:177.e9–177.e16. https://doi.org/10.1016/j.neurobiolaging.2016.12.008
30. Purandare N, Somayajulu M, Huttemann M, Grossman LI, Aras S (2018) The cellular stress proteins CHCHD10 and MNRR1 (CHCHD2): partners in mitochondrial and nuclear function and dysfunction. J Biol Chem 293:6517–6529. https://doi.org/10.1074/jbc.RA117.001073
31. Purice MD, Taylor JP (2018) Linking hnRNP function to ALS and FTD pathology. Front Neurosci 12:326. https://doi.org/10.3389/fnins.2018.00326
32. Quiros PM, Prado MA, Zamboni N, D'Amico D, Williams RW, Finley D et al (2017) Multi-omics analysis identifies ATF4 as a key regulator of the mitochondrial stress response in mammals. J Cell Biol 216:2027–2045. https://doi.org/10.1083/jcb.201702058
33. Sfakianos AP, Mellor LE, Pang YF, Kritsiligkou P, Needs H, Abou-Hamdan H et al (2018) The mTOR-S6 kinase pathway promotes stress granule assembly. Cell Death Differ 25:1766–1780. https://doi.org/10.1038/s41418-018-0076-9
34. Siegmund SE, Yang H, Sharma R, Javors M, Skinner O, Mootha V et al (2017) Low-dose rapamycin extends lifespan in a mouse model of mtDNA depletion syndrome. Hum Mol Genet 26:4588–4605. https://doi.org/10.1093/hmg/ddx341
35. Straub IR, Janer A, Weraarpachai W, Zinman L, Robertson J, Rogaeva E et al (2018) Loss of CHCHD10-CHCHD2 complexes required for respiration underlies the pathogenicity of a CHCHD10 mutation in ALS. Hum Mol Genet 27:178–189. https://doi.org/10.1093/hmg/ddx393
36. Suomalainen A, Elo JM, Pietilainen KH, Hakonen AH, Sevastianova K, Korpela M et al (2011) FGF-21 as a biomarker for muscle-manifesting mitochondrial respiratory chain deficiencies: a diagnostic study. Lancet Neurol 10:806–818. https://doi.org/10.1016/S1474-4422(11)70155-7
37. Trapnell C, Hendrickson DG, Sauvageau M, Goff L, Rinn JL, Pachter L (2013) Differential analysis of gene regulation at transcript resolution with RNA-seq. Nat Biotechnol 31:46–53. https://doi.org/10.1038/nbt.2450
38. Trapnell C, Williams BA, Pertea G, Mortazavi A, Kwan G, van Baren MJ et al (2010) Transcript assembly and quantification by RNA-Seq reveals unannotated transcripts and isoform switching during cell differentiation. Nat Biotechnol 28:511–515. https://doi.org/10.1038/nbt.1621
39. Woo JA, Liu T, Trotter C, Fang CC, De Narvaez E, LePochat P et al (2017) Loss of function CHCHD10 mutations in cytoplasmic TDP-43 accumulation and synaptic integrity. Nat Commun 8:15558. https://doi.org/10.1038/ncomms15558

Publisher's Note Springer Nature remains neutral with regard to jurisdictional claims in published maps and institutional affiliations.